Data analysis methods for the cosmic microwave background

Matthieu Tristram, K. Ganga

REVIEW ARTICLE

Data Analysis Methods for the Cosmic Microwave Background

M. Tristram[1] and K. Ganga[2]

[1] LAL; Université Paris-Sud 11, Bâtiment 200, 91400 Orsay, France
[2] APC; 10, rue Alice Domon et Léonie Duquet, 75013 Paris, France

E-mail: tristram@lal.in2p3.fr

Abstract. In this review, we give an overview of some of the major aspects of data reduction and analysis for the Cosmic Microwave Background. Since its prediction and discovery in the last century, the Cosmic Microwave Background Radiation has proven itself to be one of our most valuable tools for precision cosmology. Recently, and especially when combined with complementary cosmological data, measurements of the CMB anisotropies have provided us with a wealth of quantitive information about the birth, evolution, and structure of our Universe. We begin with a simple, general introduction to the physics of the CMB, including a basic overview of the experiments which take CMB data. The focus, however, will be the data analysis treatment of CMB data sets.

1. Introduction

1.1. History

In 1964, Penzias and Wilson discovered a roughly 3.5 K noise excess from the sky, using a communications antenna at Holmdel, New Jersey. While serendipitous, this turned out to be a detection of the Cosmic Microwave Background radiation (CMB), for which they were awarded the Nobel Prize in 1978 [Penzias & Wilson (1965)].
In 1948, Alpher and Herman had published the idea that photons coming from the primordial Universe could form a thermal bath at approximatively 5 K [Alpher & Herman (1948)], while the present general physical description of the CMB was obtained in the '60s [Dicke *et al* (1965)].

1.2. CMB radiation

In 1929, Edwin Hubble inferred that distant galaxies are moving away from us with velocities roughly proportional to their distance [Hubble (1929)]. This is now considered the first evidence for the expansion of our Universe. Given this expansion, we can assume that the Universe was much denser and hotter earlier in its history. Far enough back in time, the photons in the Universe would have had enough energy to ionize hydrogen. Thus, we believe that sometime in the past, the Universe would have consisted of a "soup" of electrons, protons and photons, all in thermal equilibrium, coupled electromagnetically via the equation :

$$e + p \leftrightarrows H + \gamma.$$

Moving forward in time from this point, the Universe expands, and the temperature decreases. The temperature will decrease to the point where there are no longer appreciably many photons which can ionize Hydrogen, so the protons and electrons will combine to form Hydrogen, and stay in this form. This is called the epoch of recombination. At this point, the photons are no longer effectively coupled to the charged particles, and they essentially travel unimpeded to this day. This is the CMB we see today.

1.3. A black body

At the time of decoupling, constituents of the Universe are in thermal equilibrium, so the electromagnetic spectrum of the CMB photons is a black body, for which the intensity is

$$I_\nu = \frac{2h\nu^3}{c^2}\frac{1}{e^{h\nu/k_BT}-1}.$$

This prediction was verified by NASA in 1989 with the FIRAS instrument on board the Cosmic Background Explorer (COBE) satellite. After a year of observation, FIRAS measured a spectrum that was in near-perfect agreement with the predictions (figure 1). A recent re-analysis of FIRAS data gives a black body temperature of 2.725 ± 0.001 K ([Fixsen & Mather (2002)]).
CMB practitioners often use the somewhat opaque "CMB", or "thermodynamic", units, assuming that small brightness variations are related to small deviations in temperature from that of the CMB as a whole. Thus, these units can be obtained from the derivative of a blackbody with respect to temperature via the equation:

$$\Delta T = T_{\rm cmb}\left(\frac{2h\nu^3}{c^2}\frac{e^{h\nu/kT_{\rm cmb}}}{\left(e^{h\nu/kT_{\rm cmb}}-1\right)^2}\frac{h\nu}{kT_{\rm cmb}}\right)^{-1}\Delta B.$$

1.4. Dipole

After removing the mean value of the CMB, one finds a dipole pattern with an amplitude of roughly 0.1% of the average CMB temperature. This is due to the doppler shift of CMB photons from the relative motion of the Solar System with respect to the rest frame of the CMB. CMB photons are seen as colder or hotter depending on the direction of observation following, to first order

$$\Delta T = T_{\rm cmb}\cdot\left(\frac{v}{c}\right)\cdot\cos\theta.$$

COBE and WMAP [Hinshaw *et al* (2006)] have measured the orientation and the amplitude of the dipole (figure 2). To first order, it is well-described by

$$\Delta T(\theta) = 3.358\times10^{-3}\cos\theta\ \text{K},$$

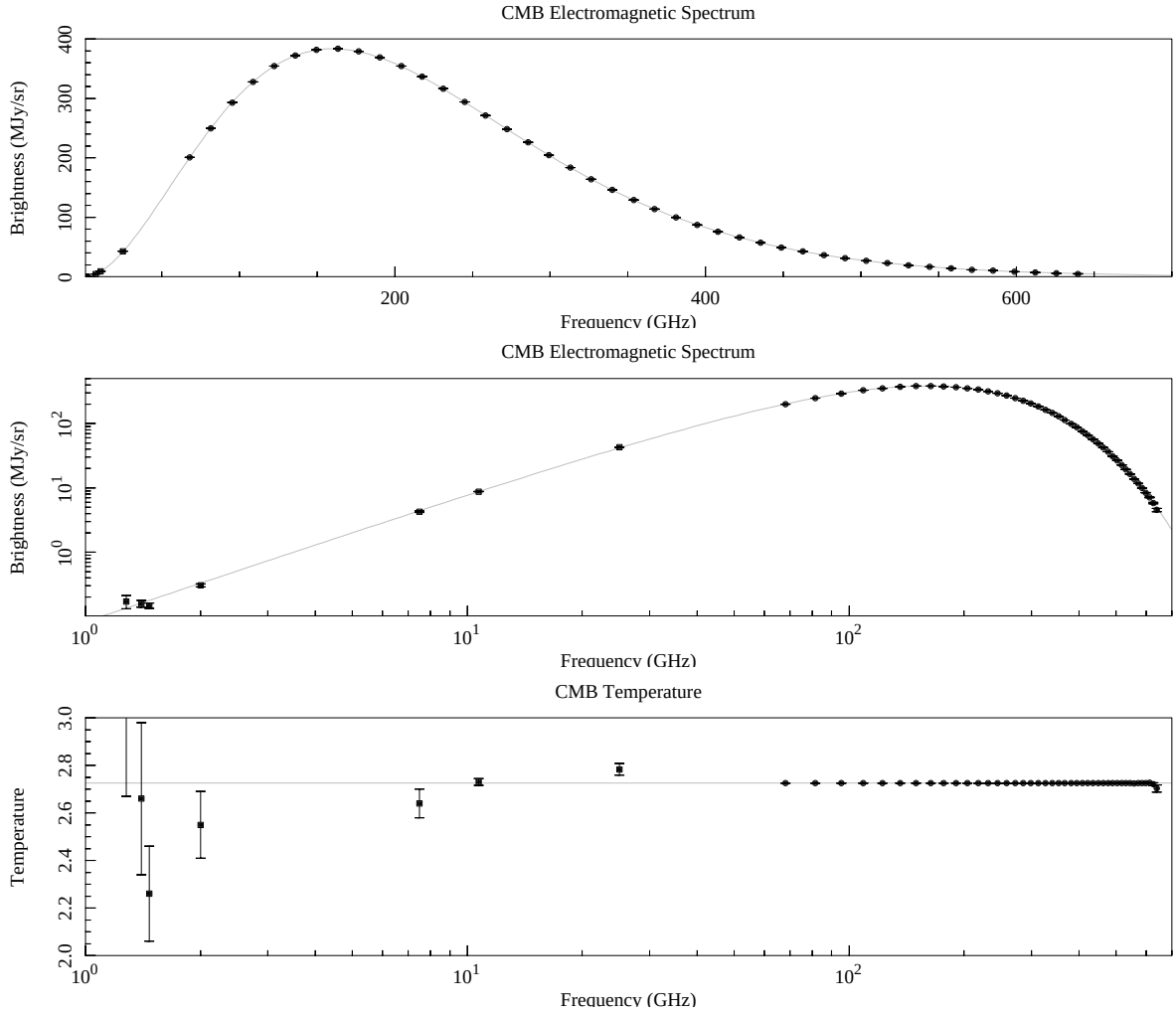

Figure 1. Electromagnetic spectrum of the CMB (top two panels) and measurements of the temperature of the CMB (bottom panel). The grey line indicates a blackbody with temperature 2.725 K. Error bars are included on all points, but in many cases are too small to discern.

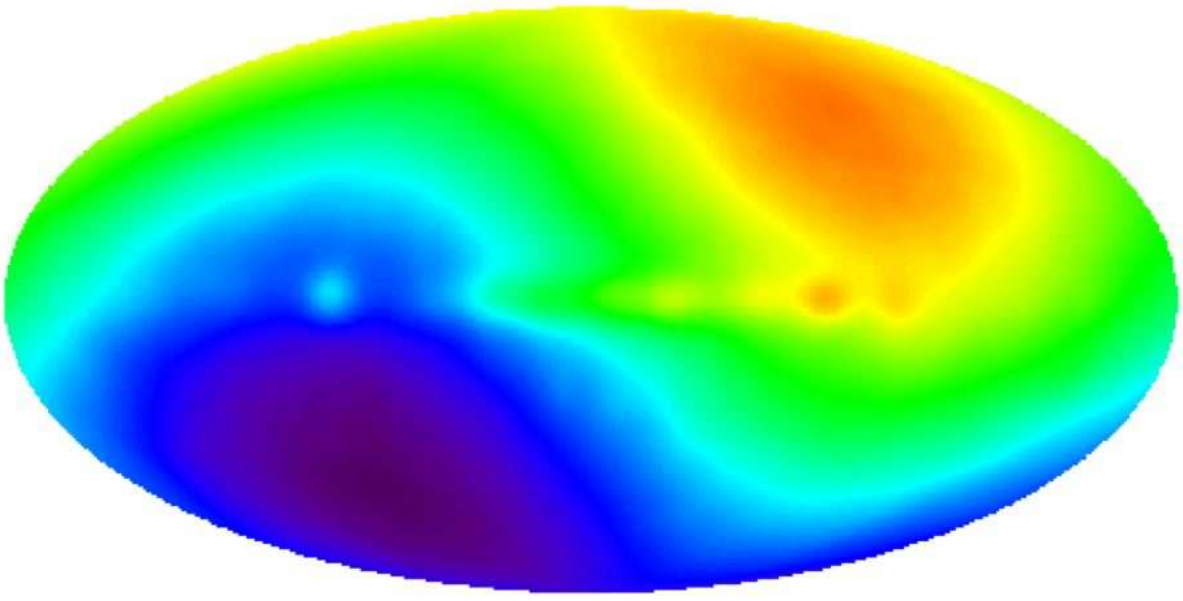

Figure 2. The CMB dipole as seen by COBE/DMR, from NASA's Legacy Archive for Microwave Background Data Analysis (http://lambda.gsfc.nasa.gov). The overall blue-to-red variation indicates the CMB dipole. The faint features in the center of the map represent the plane of our Galaxy.

where θ is the angle between the direction of observation and the dipole axis. The measured dipole implies that our Solar System is traveling at roughly 370 km/s with respect to the rest frame of the CMB. The motion of the Earth around the Sun contributes a roughly 10% modulation to this effect, which has been removed from this figure.
The motion of the Earth around the Sun also produces an additional dipole contribution. This effect is another order of magnitude lower than that of the dipole due to the motion of the Solar System with respect to the CMB rest frame. However, given that the dynamics of the Earth within the Solar System are very well understood, this signal provides a very convenient method to calibrate any CMB anisotropy measurements, if an experiment can measure these large scale variations.

1.5. Primordial anisotropies

As the Universe is expanding today, it must have been much smaller earlier in its history. It must therefore have been much hotter, meaning that both matter and the photons in the Universe had more energy. Imagine the point, very early in the history of the Universe, where the photons each have much more energy than that needed to ionize a Hydrogen atom. At this point, the matter and the photons are in good thermal equilibrium.
From this point, as the Universe cools, there are fewer and fewer photons with enough energy to ionize hydrogen. At a certain point, the mean free path of the photons becomes comparable to the size of the accessible Universe, and the protons and electrons are essentially free to combine permanently into hydrogen atoms. This period is given the rather confusing name of "recombination" – confusing since the protons and electrons have never been consistently combined until this point. From this point on, the photons are only lightly coupled to the now neutral matter – the Hydrogen atoms.
While the process of cooling is happening, imagine a volume of this photon-matter. Gravitational instatibility, seeded by some small deviation from uniformity, can cause the matter in the volume to compress. However, photon pressure will tend to push such overdensities apart. Thus, we are in a situation where structures of a given size go through a series of compactifications and rarefactions. Smaller regions will go through a series of compactifications and rarefactions before recombination. Larger regions will do so less often. These are called "acoustic oscillations" in the fluid. See figure 3
The so-called "first peak" in the power spectrum represents the scale at which matter has just had time to maximally compress before the recombination, which freezes these anisotropies into the photon signature. This next peak represents the scale at which a single compactification and a single rarefication has happened, etc.
Depending on which angular scales we are interested in, the primordial anisotropies have amplitudes of roughly one part in 100000 of the CMB mean. While quantitative estimation of the anisotropies caused by a number of effects has been done, we give below a brief description of a few of them.

1.5.1. Temperature: Depending on angular scales, one can describe three major effects which cause anisotropies in the CMB:

- Adiabatic perturbations: Quantum fluctuations in the vacuum produce fluctuations of the density ρ. In inflation theories, these perturbations are adiabatic and Gaussian. For a given density perturbation, the temperature fluctuation is

$$\frac{\Delta T}{T} = \frac{1}{3}\frac{\delta\rho}{\rho}.$$

- Gravitational perturbation (Sachs-Wolfe [Sachs & Wolfe (1967)]): When a photon falls into (or climbs out of) a gravitational well, its energy grows (or decreases) and it is thereby blueshifted (or redshifted). Thus, on the sky, matter over-densities correspond to cold spots and under-densities correspond to hot spots. It must also be remembered that the Universe is expanding during this process so that when a photon traverses a gravitational potential change, the photon will see a different potential on entry and on exit of the well or hill.
- Kinetic perturbation (Doppler): Variation of the primordial plasma velocities implies a Doppler effect on CMB photons. This shifting is proportional to the fluid velocity v, relative to the observer

$$\frac{\Delta T}{T} \propto v.$$

  This effect vanishes along the line of sight for scales smaller than the depth of the last scattering surface, but can be seen on large scales.

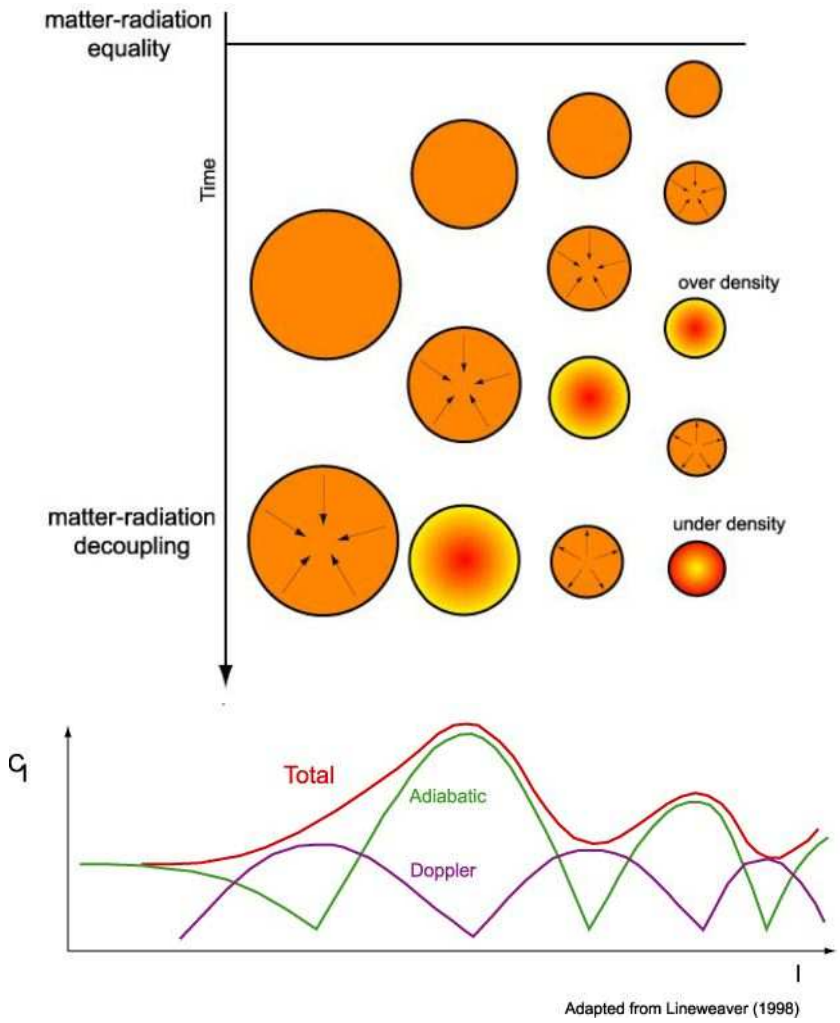

Figure 3. Acoustic oscillations and doppler peaks. Small structures come into the horizon earlier than larger ones and start oscillating. At the time of decoupling, we can observe the phase shifting of oscillations through the variation of amplitude fluctuation in temperature with respect to the size of the structures (characterized by the multipole ℓ). Figure adapted from [Lineweaver (1997)].

1.5.2. Polarization: Polarization in the primordial CMB anisotropies comes from Thomson scattering by electrons (figure 4). One can show via symmetry that only local quadrupolar anisotropies of the radiation can produce a linear polarization of the CMB photons. This is illustrated in the expression of the differential Thomson scattering cross-section of a electron on a non-polarized radiation

$$\frac{d\sigma}{d\Omega} = \frac{3\sigma_T}{8\pi}|\epsilon \cdot \epsilon'|^2.$$

Local quadrupolar anisotropies can be due to three different effects:

Scalar perturbations scalar modes from density perturbations can cause quadrupolar anisotropies. See figure 5.

Vector perturbations Vortex movements of the primordial fluid can produce quadripolar anisotropies. They are not necessarily linked to an over-density. In most of inflationary models, these perturbations are negligible.

Tensor perturbations A gravitational wave passing through a density fluctuation can modify the shape of a gravitational well. A symmetrical well become elliptical producing quadrupolar anisotropies.

1.6. Secondary anisotropies

Between the last scattering surface and our detectors, CMB photons can encounter a number of perturbations. These produce so-called "secondary" anisotropies. They are usually either gravitational

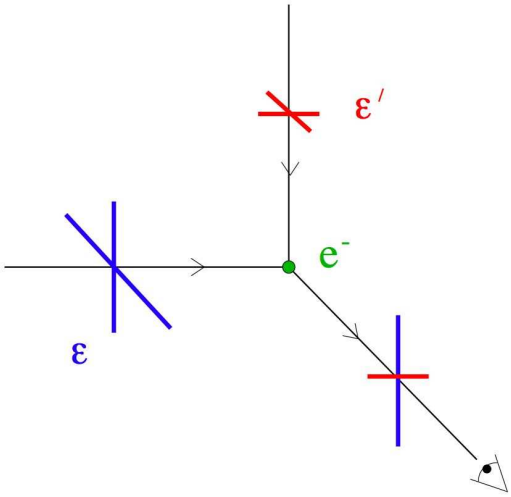

Figure 4. CMB polarization and quadrupolar anisotropies. A flux of photons with a quadrupolar anisotropy (ϵ,ϵ') scatters from an electron resulting in linearly polarized radiation.

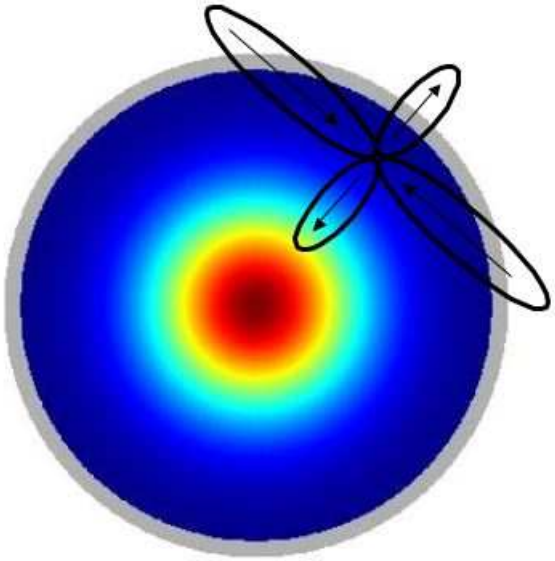

Figure 5. quadrupolar anisotropies formation on a over-dense region. Electron along the over-density radius move away from each other whereas those that belong to a same density contour get closer.

or due to Compton scattering with electrons. The effects on the angular power spectra are more fully described in [Hu *et al* (1995a)].

1.6.1. Gravitational effects:

Integrated Sachs-Wolfe: This results from the variation of the gravitational field along the path of a photon as the Universe expands. This effect is limited. It can reach $\delta T/T \simeq 10^{-6}$ at large angular scales.

Gravitational lensing: This is a distortion of the gravitational field due to massive objects (galaxies, clusters) that modify a photon's trajectory [Seljak & Zaldarriaga (2000)]. The angular power spectrum is smoothed by a few percent, which can make the small oscillations in the power spectrum at high multipoles disappear.

Rees-Sciama: [Rees & Sciama (1968)]. This is linked to the development of gravitational wells with time. Photons that fall into a well need more energy to escape it than they received when entering; that is, the photons loose energy, if the well develops. This effect arises mostly when

structures are forming. The *rms* amplitude of this effect is around $\delta T/T = 10^{-7}$ for a degree scale [Hu *et al* (1995a)]. It can reach $\delta T/T \simeq 10^{-6}$ for smaller scales (around 10 – 40 arcmin) and can even become dominant below 40 arcsec [Seljak (1996)].

1.6.2. Scattering effects:

Sunyaev-Zel'dovich (SZ) effect: This is an inverse Compton effect, in which photons increase their energy by scattering from free electrons within hot gazes inside clusters [Zel'dovich & Sunyaev (1969)], so that it is mostly significant at small angular scales. To first order, this slightly increases the energy of each photon and thus shifts the CMB electromagnetic spectrum. To second order, if the cluster is moving, one should also see a kinetic effect due to bulk motion of the cluster. At large angular scales, the SZ effect can be seen due to diffuse scattering inside our own cluster. Anisotropies can reach $\delta T/T \simeq 10^{-4}$ for scales that range between a degree and arc-minutes.

Reionization: This corresponds to a period where the Universe becomes globally ionized once again, after recombination [Gunn & Peterson (1965)]. During this period, free electrons will once again scattered CMB photons. It probably appears during structure formation ($z = 6 - 20$). The effect on the CMB is visible both at small angular scales (suppressing the power from clusters) and at large scales.

1.7. Foregrounds

CMB measurements can be contaminated by other astrophysical emissions arising from our neighborhood [Bouchet & Gispert (1999)]. Some examples are:

- **Synchrotron emission.** Relativistic electrons accelerated by a magnetic field produce synchrotron radiation, with a spectrum depending on both the intensity of the magnetic field and energy and flux of the electrons. The Galactic magnetic field of order a few nG is strong enough to produce this effect. The energy spectrum of the electrons is usually modeled as a power law, $\nu^{-\beta}$, with $\beta \simeq 3$ [de Zotti *et al* (1999)]. Synchrotron is the dominant foreground for for lower CMB frequency observations.
- **Bremsstrahlung (or *free-free*) radiation.** In a hot gas, ions decelerate free electrons, thereby producing thermal radiation. Once again, the *free-free* spectrum can often be modeled as a power law with spectral index $\beta \simeq 2.1$ [de Zotti *et al* (1999)]. As with synchrotron, *free-free* emission is most evident at lower CMB frequencies.
- **Galactic dust emission.** Cold dust within our own Galaxy can emit via thermal radiation (*vibrational dust*) or by excitation of their electrical dipolar moment (*rotational dust*). Thermal radiation is modelled as a grey body at $T \sim 17$ K, with an emission maximum in the far-infrared. In the radio-millimetric domain, the dust emissivity can be modeled as ν^2 [Schlegel *et al* (1998)]. Vibrational dust emission has been claimed to have been seen between 10 and 100 GHz and with a maximum around 20 GHz [Watson *et al* (2005)], though there is still debate.
- **Extragalactic point sources.** Some point sources can emit in the radio-millimetric domain. To avoid contamination by these, they are masked before the CMB power spectrum is estimated. For the background of undetected sources, their effect on the CMB spectrum is evaluated with Monte Carlos.

Figure 6 shows representative foreground spectra, though they may vary depending on location on the sky. CMB experiments usually measure the CMB in the window between ∼20 and 300 GHz, while measurements at higher and lower frequencies help estimate and limit the level of foreground contaminants within a the CMB band.
While some experiments have measured polarized foregrounds, notably Parkes [Giardino *et al* (2002)] and WMAP [Barnes (2003)] for synchrotron and free-free and ARCHEOPS for diffuse dust emission on large angular scales [Benoît *et al* (2004), Ponthieu *et al* (2005)], foreground polarization over the full sky are still not well known. Thus foreground residuals have become one of the largest (if not the largest) source of systematic errors in CMB analyses.

1.8. Angular power spectra

To describe CMB anisotropies, we decompose both temperature and polarization sky maps into spherical harmonics coefficients. Most inflationary models predict fluctuations that give gaussian anisotropies in the linear regime [Hu *et al* (1997), Linde *et al* (1999), Liddle & Lyth (2000)]. In such

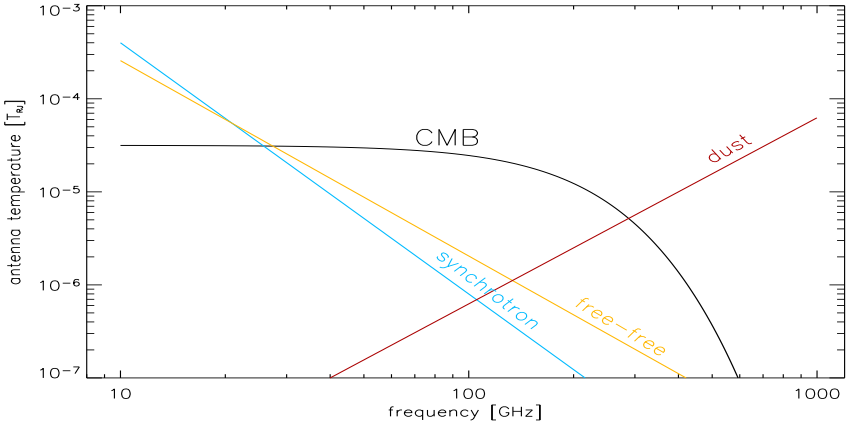

Figure 6. Foregrounds spectra compared to CMB one (*black*). Amplitudes are normalized to the Sachs-Wolfe plateau. Synchrotron (*blue*) and *free-free* (*yellow*) are dominating at low frequency until ∼30 GHz. Dust (*red*) is dominating at higher frequency (above 300 GHz).

cases, the angular power spectra both in temperature and polarization contain all the cosmological information of CMB.

1.8.1. Temperature: The spherical harmonics, $Y_{\ell m}$, form an orthogonal basis defined on the sphere. The decomposition of a scalar map into spherical harmonic coefficients $a^T_{\ell m}$ reads

$$\frac{\Delta T\left(\vec{n}\right)}{T} = \sum_{\ell=0}^{\infty} \sum_{m=-\ell}^{\ell} a^T_{\ell m} Y_{\ell m}\left(\vec{n}\right),$$

where $a^T_{\ell m}$ satisfy

$$a^T_{\ell m} = \int \frac{\Delta T\left(\vec{n}\right)}{T} Y^*_{\ell m}(\vec{n}) d\vec{n}.$$

The multipole ℓ represent the inverse of the angular scale. We can define the angular power spectrum C^T_ℓ by

$$C^T_\ell = \left\langle |a^T_{\ell m}|^2 \right\rangle$$

Moreover, for gaussian anisotropies, the $a_{\ell m}$ distribution is also gaussian and its variance is the angular power spectrum C_ℓ:

$$\begin{aligned} \langle a_{\ell m} \rangle &= 0, \\ \langle a_{\ell m} a_{\ell' m'} \rangle &= C_\ell \delta_{\ell \ell'} \delta_{m m'}. \end{aligned}$$

Thus we can write an estimator $\tilde{C}^T_\ell$ of the power spectrum that reads

$$\tilde{C}^T_\ell = \frac{1}{2\ell+1} \sum_{m=-\ell}^{\ell} a^T_{\ell m} a^{T*}_{\ell m}.$$

The angular power spectrum in temperature shows three distinct regions (see figure 7):

(i) **The Sachs-Wolfe plateau.** For scales larger than the horizon, causality dictates that fluctuations never evolve. Anisotropies come from initial fluctuations of photons (form the gravitational field) and from the Sachs-Wolfe effect [Sachs & Wolfe (1967)]. Since the spectrum of the fluctuations from the gravitational field is scale invariant, the temperature fluctuations are statistically identical and the angular power spectrum is nearly flat at large scales (small multipole ℓ).

(ii) **Acoustic oscillations.** For scales smaller than the horizon, in a matter dominated Universe, the fluid undergoes acoustic oscillations that are adiabatic. Baryons fall into gravitational wells, whereas photon radiation pushes them apart. This induces acoustic oscillations of matter which imprints on the photons. Structures enter the horizon progressively (starting with the smallest ones) resulting in a progression of oscillations depending on the size of the structures (fig 3). Peaks in the angular power spectrum reflect these phase-differences for scales smaller than the horizon ($\ell \gtrsim 180$). Differences in the electron velocities at the time of the last scattering also imply a second order Doppler effect.

(iii) **Damping region.** At still smaller angular scales, the spectrum is damped, mainly due to residual diffusion of photons, which smooths structures with scales smaller than the mean free path (Silk damping). Furthermore, the recombination process is not instantaneous, with a finite width resulting in a more gradual damping.

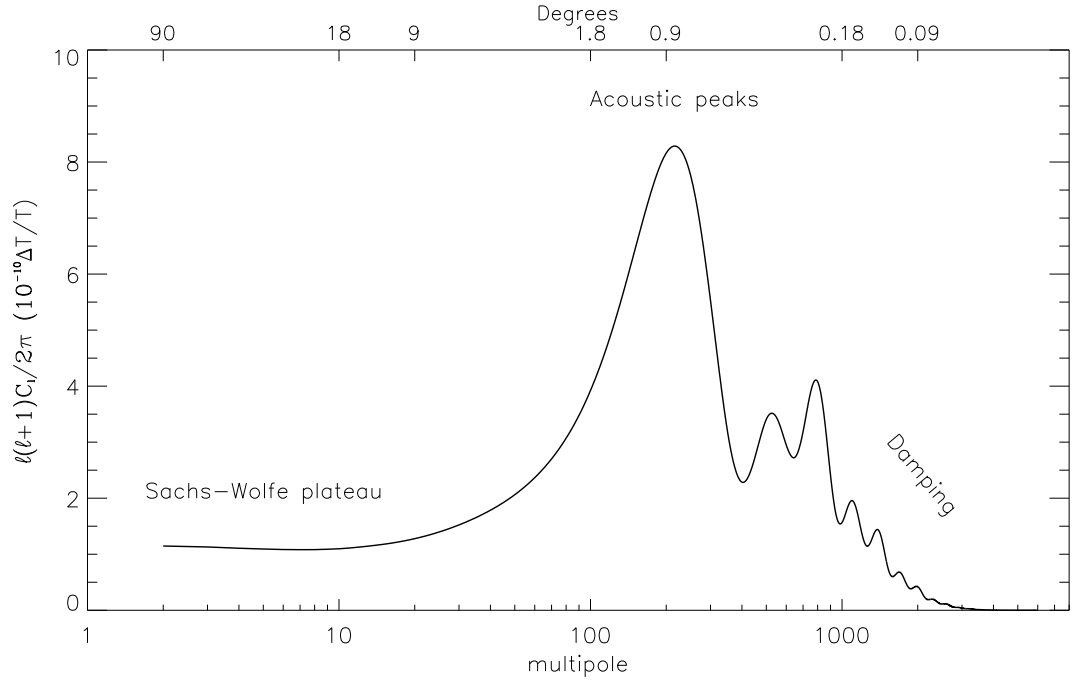

Figure 7. Temperature angular power spectrum: power on the sky as a function of the multipole ℓ or angular scales. We can distinguish three regions from left to right: the Sachs-Wolfe plateau, the acoustic peaks and the damping region.

The correlation function of the signal on the sky is

$$C(\theta) = \sum_{\ell} \frac{2\ell+1}{4\pi} C_\ell P_\ell(\cos\theta)$$

We note that the power spectra are often plotted as

$$f(C_l) = \frac{l(l+1)}{2\pi} \cdot C_l.$$

This is convenient, as when shown like this the area under the curve is roughly equal to the variance of the signal on the sky.

1.8.2. Polarisation: The Stokes formalism allows one to describe polarized radiation with four scalars: I, Q, U and V. For a polarized wave propagating along the z axis, Stokes parameters are

$$\begin{aligned} I &= \left\langle |E_x|^2 + |E_y|^2 \right\rangle, \\ Q &= \left\langle |E_x|^2 - |E_y|^2 \right\rangle, \\ U &= \left\langle 2Re(E_x E_y^*) \right\rangle, \text{ and} \\ V &= \left\langle 2Im(E_x E_y^*) \right\rangle. \end{aligned}$$

Unpolarized light is described by $Q = U = V = 0$. Q and U characterize the linear polarization for the photon whereas V describes the circular polarization. I and V are rotation invariant whereas Q and U depend on the frame of reference.. Conservation of the total energy of a wave implies that

$$I^2 \geq Q^2 + U^2 + V^2.$$

Stokes parameters can be summed for a superposition of incoherent waves. Thomson diffusion cannot create circular polarization as it does not modify the phases but only the amplitudes of each component. Thus, for CMB, $V = 0$.

In the same way as for temperature, we can define polarized angular power spectra using the decomposition in spherical harmonics for the Q and U parameters on the sky. To do this, we use the scalar E and pseudo-scalar B quantities defined from Stokes parameters but which are independent from the frame of reference. The decomposition is made using the spin-two harmonics:

$$(Q \pm iU)(\vec{n}) = \sum_{\ell m} a_{\pm 2 \ell m} \, {}_{\pm 2}Y_\ell^m(\vec{n}).$$

The connection between Q/U and E/B in spherical harmonic space is

$$\begin{aligned} a_{\ell m}^E &= -\frac{a_{2\ell m} + a_{-2\ell m}}{2} \\ a_{\ell m}^B &= i\frac{a_{2\ell m} - a_{-2\ell m}}{2}, \end{aligned}$$

where we can define the purely polarized angular power spectra C_ℓ^E and C_ℓ^B as

$$\begin{aligned} C_\ell^E &= \langle |a_{\ell m}^E|^2 \rangle \\ C_\ell^B &= \langle |a_{\ell m}^B|^2 \rangle. \end{aligned}$$

Polarization of the CMB is due to quadrupolar anisotropies at the last scattering surface. We thus expect correlations between temperature anisotropies and polarized anisotropies, which can be described by the temperature-polarization angular cross-power spectra

$$\begin{aligned} C_\ell^{TE} &= \langle a_{\ell m}^T a_{\ell m}^{E*} \rangle \\ C_\ell^{TB} &= \langle a_{\ell m}^T a_{\ell m}^{B*} \rangle. \end{aligned}$$

Finally, second-order spin spherical harmonics properties implies that

$$C_\ell^{EB} = \langle a_{\ell m}^E a_{\ell m}^{B*} \rangle = 0.$$

One can demonstrate that for scalar perturbations $E \neq 0$ and $B = 0$, whereas for tensor perturbations $E, B \neq 0$. Thus detecting B polarization in the CMB could indicate the presence of tensor modes and thus be an indication of gravitational waves.
As with the temperature spectra, polarized spectra also show peaks for scales smaller than approximately a degree (see figure 8). These are sharper for polarization, as they are due to velocity gradients of the photon-baryon fluid at the time of decoupling only (Doppler oscillation). Consequently, they are shifted by $\pi/2$ with respect to temperature peaks, which are dominated by density fluctuations. The correlation between the two is characterized by the cross temperature-polarization power spectrum C_ℓ^{TE}. The E spectrum is at the level of a few percent of the temperature spectrum. The amplitude of the B modes are still unknown but should be at least one or two order of magnitude below that of the E modes. On large angular scales, the B-mode amplitude is strongly linked to the energy of inflation E_{inf} [Zaldarriaga (2002)]:

$$[\ell(\ell+1)/2\pi]\, C_\ell^B \simeq 0.024^2 \left(E_{inf}/10^{16}\right)^4 \mu\mathrm{K}^2.$$

For gaussian fluctuations, we can also define the estimators for each spectrum:

$$\begin{aligned} \tilde{C}_\ell^E &= \frac{1}{2\ell+1} \sum_{m=-\ell}^{\ell} |a_{\ell m}^E|^2 \\ \tilde{C}_\ell^B &= \frac{1}{2\ell+1} \sum_{m=-\ell}^{\ell} |a_{\ell m}^B|^2 \\ \tilde{C}_\ell^{TE} &= \frac{1}{2\ell+1} \sum_{m=-\ell}^{\ell} a_{\ell m}^T a_{\ell m}^{E*} \\ \tilde{C}_\ell^{TB} &= \frac{1}{2\ell+1} \sum_{m=-\ell}^{\ell} a_{\ell m}^T a_{\ell m}^{B*}. \end{aligned}$$

1.8.3. Cosmic and sample variance: For both temperature and polarization, the $a_{\ell m}$ coefficients are gaussian distributed with a mean of zero and a variance given by the C_ℓ. Each of these coefficients has $2\ell + 1$ degrees of freedom, corresponding to the $2\ell + 1$ m-values for a given ℓ, due to the fact that

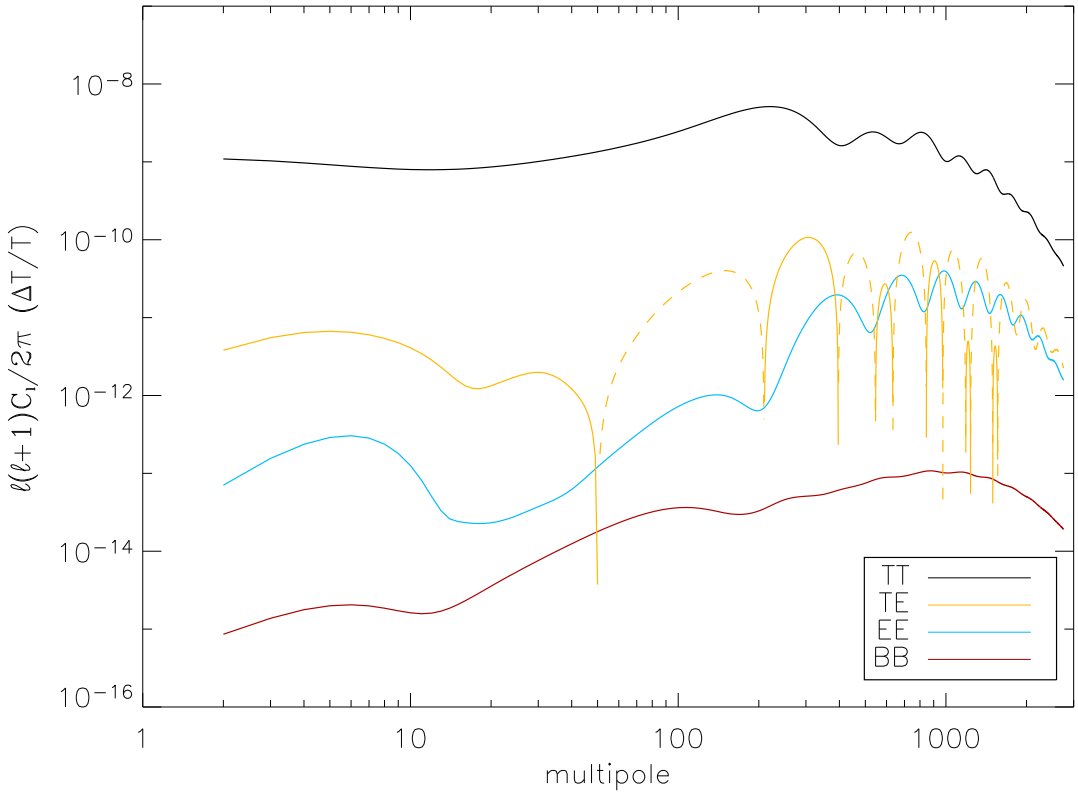

Figure 8. Angular power spectra both in temperature, polarization and cross temperature-polarization. *From top to bottom :* temperature TT, cross-spectrum TE, purely polarized spectrum E et an optimistic estimation of the B spectrum.

we can only measure a single realization of our Universe from one location. This induce an intrinsic variance on the estimated C_ℓ, called cosmic variance that is equal to

$$Var_{cosmic}(\tilde{C}_\ell) = \frac{2}{2\ell+1} C_\ell^2.$$

Note that for large angular scales, this can become significant.
Moreover, CMB anisotropies measurements cannot cover the whole sky. Even for satellites, foreground emission residuals can be comparable to the CMB signal and we therefore must use a mask that reduces the effective coverage. For each multipole, the number of degrees of freedom increase as a function inverse of the observed area f_{sky} and so the associated variance (called sample variance)

$$Var_{sample}(\tilde{C}_\ell) = \frac{2}{(2\ell+1) f_{sky}} C_\ell^2.$$

2. Instruments

2.1. Observation sites

CMB experiments have observed the CMB from a variety of different sites; from telescopes sited all over the globe, to balloons, to satellites in Earth orbits, and now even to satellites at the second Sun-Earth Lagrange point. Each site has its own advantages and disadvantages. Specifically:

- Sky coverage: Full-sky coverage is usually only achieved by satellites, which have the unique combination of long observation times and unobstraucted views of the sky. Balloon-borne experiments can cover a significant fractions of the sky (such as ∼30% for Archeops [Benoît *et al* (2003)] and FIRS [Ganga *et al* (1993)]). The balloon-borne 19 GHz experiment [Boughn *et al* (1992)] covered almost the full sky by making multiple flights from North American and Australia, but balloon observations are often limited to much smaller regions (for example,

<10% of the sky for BOOMERanG or 0.25% for MAXIMA [Rabii *et al* (2006)]). Ground base measurements can usually only cover a few percent of the sky.

- Resolution: Detector resolution is directly linked to the size of the telescope and the wavelength of observation. Satellites and balloons are thus usually limited in resolution compared to ground-based measurements due to weight constraints.
- Atmosphere: Satellite, obviously, do not have problems with terrestrial atmosphere. Ground-based measurements, on the other hand, are hampered by atmospheric emissions such as water vapor, which absorbs microwave radiation. Thus ground base telescopes for the CMB are operated from dry, high altitude locations such as the Chilean Andes or the South Pole. Balloon experiments, flying at tens of kilometers from the ground, offer a compromise. Nevertheless, there are still some atmospheric effects from, for example, ozone clouds.
- Observing time: Balloon-borne CMB experiments have usually been single-night observations, though some experiments have had multiple flights, and so-called "long duration" flights of over a week are now becoming common. Satellite experiments have observed for a number of years. Ground-based experiments have also observed for years.

2.2. Scanning strategy

With a given amount of observing time, which is often limited by site conditions or resources, a CMB experiment's scanning strategy aims to:

- minimize foreground contributions
- provide the redundancy necessary to analyze noise and other unforeseen effects.
- provide the best possible calibration and instrumental characterization. E.g., quasars for pointing reconstruction.
- minimize atmospheric effects
- allow a decent measurement of the power spectrum.

2.2.1. Foregrounds: As noted in section 1.7, foreground emission can be a major contaminant to CMB measurements. Thus, all CMB experiments take care to either avoid observing regions with excessive foreground emission, or to reject these regions when the data are analyzed.
To this point, all satellite-based CMB experiments have used scanning strategies which covered the entire sky, motivated by a combination of technical simplicity, and the fact that it is one of the few ways to consistently measure the largest scale anisotropies in the CMB. However, this means that some regions, such as the Galactic plane, are not useable, and must be excised from the data. Balloon experiments such as the 19 GHz Experiment [Boughn *et al* (1992)], FIRS [Ganga *et al* (1993)] and Archeops [Benoît *et al* (2003)] have been used to make large fractions of the sky. In these experiments, the Galactic plane is treated in much the same way as for satellites, with data in high-foreground regions simply avoided in the analyses.
A number of balloon-borne experiments, however, have been used to make maps of localized regions of a few percent of the sky. In such cases, the observation fields are chosen to coincide with low emission from our Galaxy. In addition, almost all ground-based experiments map but a few percent of the sky at most, and use the same foreground avoidance technique. An example of this is shown in figure 9.

2.2.2. Redundancy: It is notoriously difficult to keep sensitive experiments stable for long periods of time, and these experiments are no exception. Temperature and atmospheric changes, as well as a host of other experimental possibilities conspire to allow the baselines, or zeros of these experiments to change. If only a single measurement were made of each point on the sky, it would be quite difficult to differentiate between sky signals and so-called "systematic" effects. It would also be difficult to differentiate between "real" signal and "random noise".
To this end, experiments endeavor to observe a given part of the sky in as many different ways as possible. It is highly desirable to observe all points measured on as many different time scales as possible, from as many different directions as possible.
Note that while it is desireable to observe a given spot in as many different directions as possible, there are often overriding concerns. As an example, we note that most ground-based and many balloon experiments try to observe without changing the elevation of observations, since changing elevation with change the column depth of atmosphere through which the experiment is observing and will thus change loading and equilibrium of the experiment. Often an experiment can get "cross-linking" in various scans, since as the Earth rotates a given scanning will "rotate" on the sky. There are,

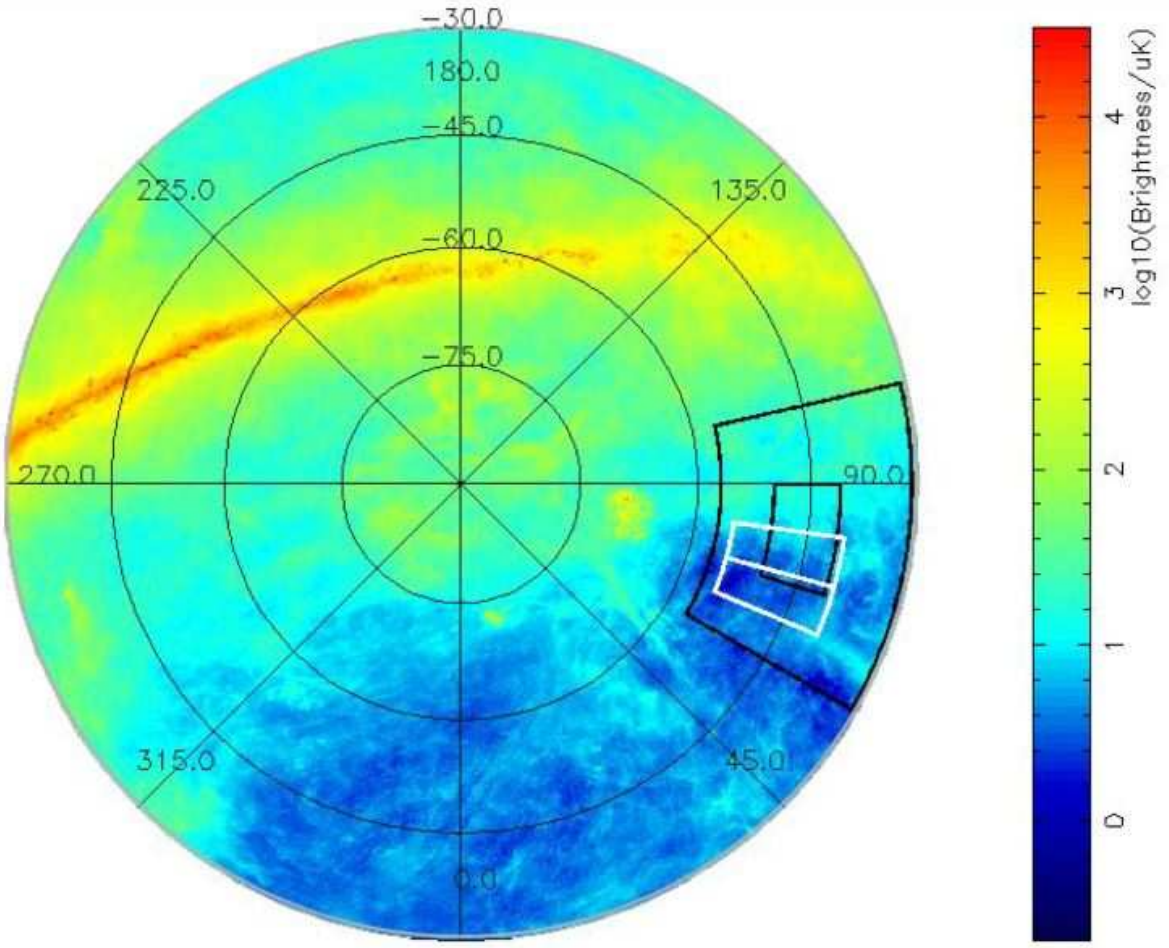

Figure 9. This grapic shows an estimate of the emission from dust which would be seen by polarization-sensitive experiments at 150 GHz. The center of the plot is the zenith at the South Pole – that is, declination -90 degrees. The edge of the plot is -30 degrees (that is, it shows the "bottom" of the celestial sphere). Zero right ascension is down in the plot, increasing in the counter-clockwise direction. The brightness estimates come from application of a model by Finkbeiner et al. [Finkbeiner *et al* (1999)]. The boxes to the right represent the sky coverage for QUaD and BOOMERanG, two CMB anisotropy experiments. The larger and smaller black boxes are the BOOMERanG so-called "shallow" and "deep" fields, respectively. The two white boxes are the two fields QUaD observed in their first season of observations [Hinderks (2005)].

however, a number of experiments which are making, or have made, observations from the South Pole. From this unique vantage point (along with the North Pole, though there have not been any CMB experiments fielded there for obvious reasons), as the earth rotates, one cannot change declinations except by changing elevations. Thus, these experiments live without the benefits of cross-linking. From the South pole, however, it is often noted that the atmosphere is low enough that experiments can work without it.

2.2.3. Calibration: While it is possible to calibrate an instrument using special techniques, by far the most accepted procedure is to use astronomical sources to calibrate, preferable sources which can be seen as part of the routine observations done of the CMB. In this way the experiment is calibrated in the configuration used to make the cosmological measurements themselves, and assumptions or extrapolations between the "routine" measurements and the calibration measurements need not be made.

The most desirable source to use would be something with the frequency spectrum of the CMB anisotropies themselves. While an increasing number of experiments are using the CMB anisotropies themselves, as measured by previous experiments, to calibrate, a number of experiments have also used the CMB dipole, which also has the same spectrum. When doing this, care must be taken to account for the roughly 10% variation in the dipole due to the motion of the Earth around the Sun.

For experiments which do not cover a large enough area to use the dipole for calibration, the scanning strategy will ideally cover a planet or some bright, well-known point source which, along

with understanding of the beam and bandpass of the instrument, can provide a flux calibration. In addition, these sources can be used to refine pointing and beam models.

2.2.4. Power Spectrum Sampling: Different regions of the power represent structures of different sizes – lower multipoles representing structure at larger angular scales and higher multipoles representing structure at smaller angular scales. For experiments interested in measuring the structure on the largest scales, the scanning strategy must, of course, cover areas of these sizes. In addition, in order to have sufficient statistics, the experiment will usually have to cover a number of patches of the size of interest, in order to integrate down the "sample variance" [Scott *et al* (1994)], the inherent variance we will find from one patch of a given size to another, even when the fluctuations in both are given by the same underlying model.
In addition, if one fails to observe large enough regions, even if one can formally measure power spectrum values for a given multipole, without enough observations the spectrum points at different multipoles will be *correlated*, effectively limiting the experiments resolution in multipole space [Tegmark (1996b)].

2.3. Detectors

2.3.1. Low Frequency: Here, "Low Frequency" refers to frequencies between roughly 15 and 95 GHz. From the COBE Differential Microwave Radiometer (DMR) and the Wilkinson Microwave Anisotropy Probe (WMAP), to the low frequency instrument (LFI) of Planck, we can see three examples of low frequency radiometers.
A radiometer is a device whose output voltage is proportional to the power received by a horn antenna. The output is then sent to an amplifier such as a High Electron Mobility Transistor (HEMT). For radiometers sensitive to polarization, one can use an OrthoMode Transducer (OMT) to separate the orthogonal polarizations with minimal losses and cross-talk. The two orthogonal linear polarizations are then directed into separate amplifiers.
The radiometer equation [Dicke *et al* (1946)]

$$\delta T = T_{sys}\sqrt{\frac{1}{\Delta\nu\tau} + \left(\frac{\Delta G}{G}\right)^2},$$

gives the total power radiometer's sensitivity for an integrating period τ, a frequency-dependent power response $G(\nu)$, an input referenced system noise temperature T_{sys} and the effective RF bandwidth $\Delta\nu = \left[\int G(\nu)d\nu\right]^2 / \int G^2(\nu)d\nu$. The second term represents the noise coming from the gain variation of the radiometer during the integration time τ.
Due to their low noise and wide bandwidth, HEMTs are good candidates for measurements of the CMB. Unfortunately, these amplifiers exhibit long scale variations of their gain that limit sensitivity of the radiometers. Reducing 1/f noise can be done using differential radiometers. That is, by switching the inputs from two antennas or an antenna and a reference load, the temperature of which is close to the measured signal (as for Planck-LFI). In the first case, difference signal is then constructed using two orthogonally polarized channels. In the second case, a hybrid coupler can provide two phase-switch signals from the reference load and the sky signal. In both cases, switching enhances the instrument's performances in two ways: (1) since both signals are amplified by the same chains, gain fluctuations in either amplifier chain act identically on both signals so that common mode gain fluctuations cancel; (2) the phase switches introduce a 180° relative phase change between two signal paths. Thus, low frequency (1/f) noise is common mode and vanishes.
These low frequency radiometers are usually cooled to lower than 100 K, which reduces amplifier noise and makes them more sensitive.
The DMR was launched in 1989. It detected structure in the CMB angular distribution at angular scales $\gtrsim 7°$ [Smoot (1990)], using two Dicke-switched radiometers at frequencies: 31, 53 and 90 GHz, with noise temperature of 250, 80 and 60 times the quantum limit respectively, fed by pairs of feed horns pointed at the sky.
WMAP [Jarosik *et al* (2003)] was launched in June of 2001 and is currently observing the sky in five frequency bands: 23, 33, 41, 61 and 94 GHz, with arrays of radiatively-cooled radiometers fed by a differential two-telescope optical system. Radiometer noise temperatures are 15–25 times the quantum limit, with angular resolution ranging from 56 arcmin to 14 arcmin.
The LFI instrument, slated to fly on the Planck satellite [Bersanelli & Mandolesi (2000)], with its array of cryogenically cooled radiometers, represents another advance in the state of the art. It is designed to produce images of the sky (including polarized components) at 30, 44 and 70 GHz, with high sensitivity.

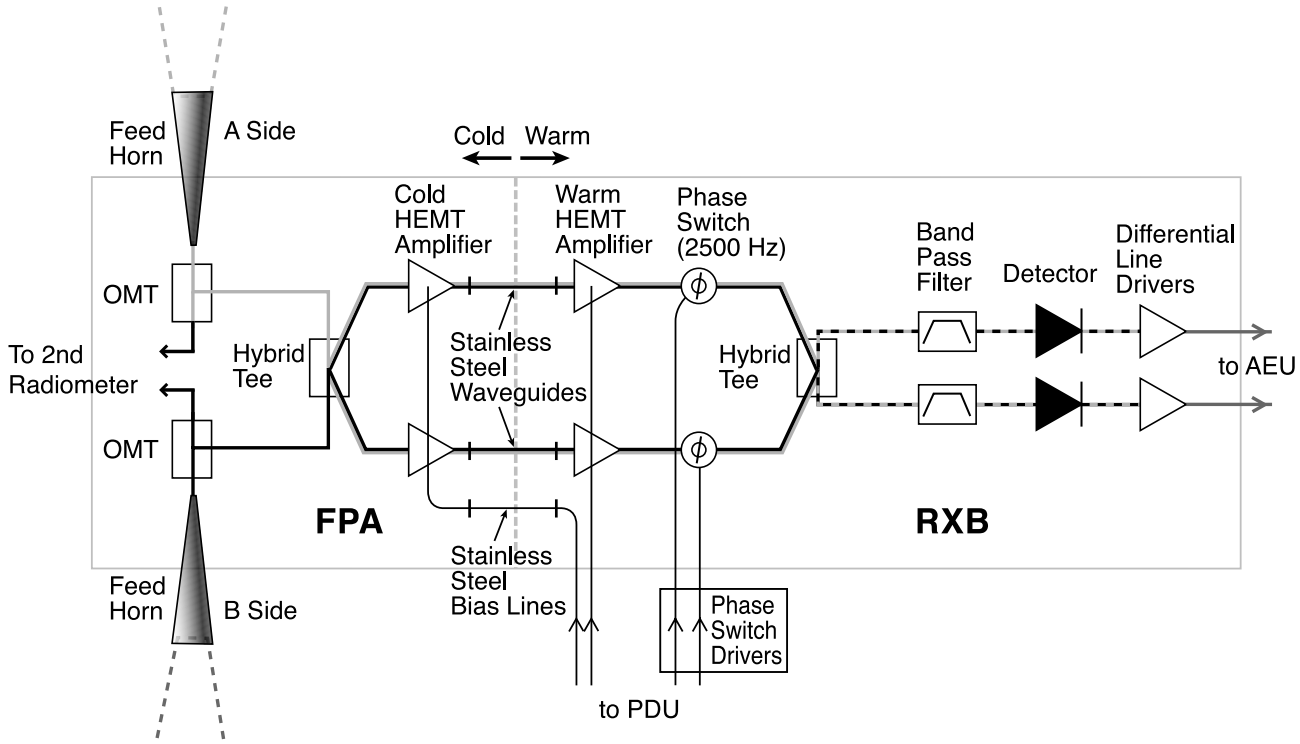

Figure 10. Layout of an individual WMAP radiometer. Components on the cold (*left*) side of the stainless steel waveguides are located in the FPA and are passively cooled to 90 K in flight. (figure extracted from [Jarosik *et al* (2003)])

2.3.2. High Frequency: Here, "High Frequency" refers to frequencies between roughly 95 and 250 GHz. Bolometric detectors [Chanin & Torre (1983)] are micro-fabricated devices in which the incoming radiation is absorbed by a grid, causing an increase in temperature. This temperature increase is measured by a Neutron Transmutation Doped (NTD) germanium thermistor, which provides high sensitivity with sufficient stability. These detectors give extremely high performance, yet are insensitive to ionizing radiation and microphonic effects.
The modern "total power" CMB bolometers are grids which resemble spider webs (figure 11), with characteristic scales related to the wavelength of the radiation of interst, reducing background coming from lower wavelengths. Moreover, this configuration enhances sensitivity and reduce the time response and cross-section with particles. Its lower mass gets him less sensitive to vibration. For Polarization-Sensitive Bolometers (PSB), radiation is absorbed by two orthogonal grids of parallel resistive wires, each of which absorbs only the polarized component with electric field parallel to the wires [Jones *et al* (2003)]. Polarized sky can be reconstructed using several detector measurements.
Radiation from the telescope is coupled to the bolometer via horns and filters to select the wavelength. Thermodynamic sources of noise in a bolometer are coming from :

(i) phonon noise proportional to temperature;
(ii) Johnson noise linked to fluctuations of tension applied on the thermistor;
(iii) photon noise coming from quantic nature of the incoming radiation.

The fundamental limit of the sensitivity of a bolometer is phonon noise in the thermal link between the absorber and the heat sink. In this case, the noise equivalent power reads

$$NEP = \gamma\sqrt{4k_B T^2 G},$$

where G is the thermal conductance, T the temperature of the bath, and γ takes into account the contribution from Johnson noise in the NTD Ge thermistor. For a given background load Q, maximum sensitivity is achieved for $G \sim Q/T$ [Mather *et al* (1984)]. The time constant of the bolometer is defined by $\tau = C/G$ where C is the heat capacity of the bolometer. The time constant is fixed by the modulation scheme, putting a limit on the thermal conductance G.
Cooling down the system reduces the two first sources of noise such that intrinsic photon noise become dominant. Other sources of noise are microphonic noise coming from vibrations and 1/f noise due to low thermal drifts.

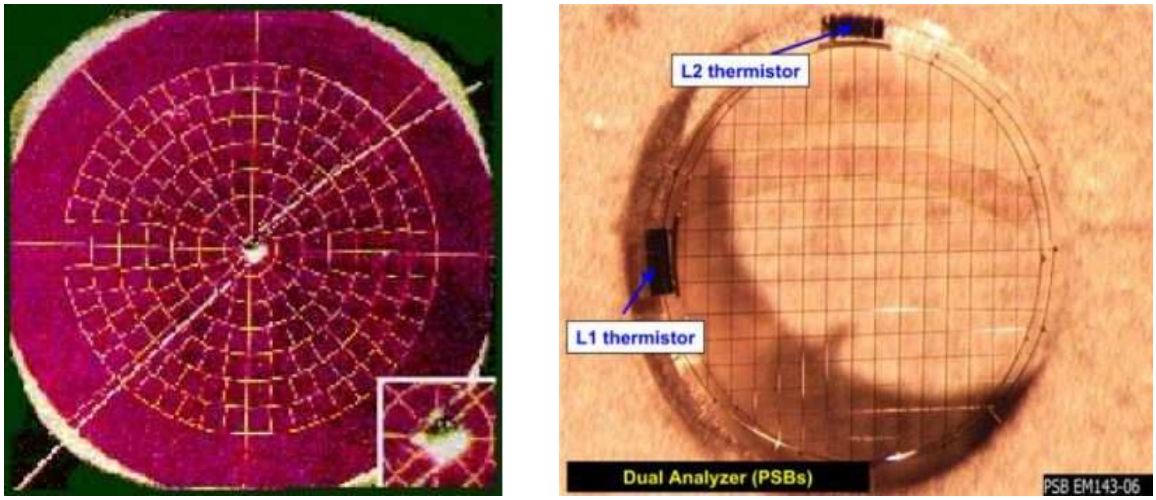

Figure 11. Spider-Web Bolometer (*left*) and Polarization-Sensitive Bolometer (*right*) from Planck High Frequency Instrument.

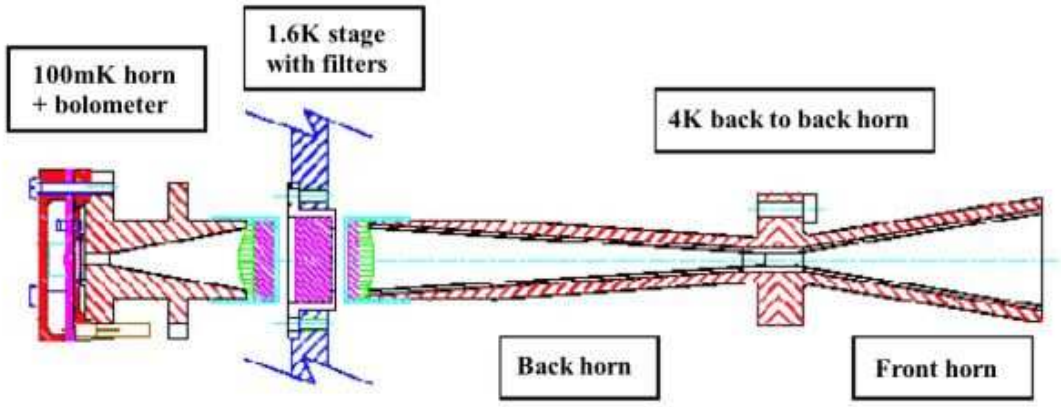

Figure 12. Optical configuration for a single photometric pixel from Archeops or Planck focal plane.

Using bolometers impose a cryogenic system to cool down detectors. BOOMERanG [Crill *et al* (2003)] uses a cryostat that operate at 270 mK. Archeops [Benoît *et al* (2002)] and Planck use a dilution cryostat that insure 100 mK on the focal plane.

2.4. Environment effects

2.4.1. Thermal effects: Detectors used for accurate measurements of temperature variations such as CMB anisotropies are very sensitive to thermal variation of he environment. Thus experiments are designed to minimize the effects of thermal variations across the focal plane and electronics which might induce changes in the gain and offsets of the detectors. The observatory environment is designed to be as stable as possible given other the other constraints of the observations. Satellites are now placed at the second Sun-Earth Lagrange point, placing the Earth between the Sun and the payload. Moreover, the focal plane is looking in the opposite direction from the Sun and large baffle prevent from most of scattering light that could enter the instrument. Balloon also used scanning strategy that avoid Sun or fly during the arctic night. Ground-based experiments prevent with the Sun light using baffles and operates during the night.
Anyway, thermal effects, that represent the largest source of systematics at low frequency, are monitored using thermometers that are used in the data analysis. The latter can also be used to regulate some of the cryogenic stages.

2.4.2. Electrical effects: Variation of electrical signal can affect the signal even for stable thermal environment. These variations can be due to, for example, solar flares, RF noise or voltage fluctuation. Signal from a detector can also be related to another one via electrical cross-talk that can be due to nonideal behavior of electronics or pickup in the wiring hardness.
Usually, tests are made at ground before the observing period to search for some parasitic effects.

2.5. Interferometers

The study of CMB anisotropies using interferometers goes back over two decade. Nowadays, high resolution measurements of the CMB power spectra have been made by ground based interferometers VSA [Dickinson *et al* (2004)], DASI [Leitch *et al* (2005)], CBI [Rajguru *et al* (2005), Readhead *et al* (2004)].
In contrast with thermometers that measure the total or differential power, an interferometer directly measures the power spectrum of the sky. Images of the sky can then be reconstructed using aperture analysis. They can cover continuously a large range of the power spectrum since their angular resolution is determined by the number of fields observed. Moreover, the detection of only correlated signals made them very stable to systematics such that ground pickup and atmospheric emission.
An interferometer measures the average over a time long (compared to the wavelength) of the electric fields vectors E_1 and E_2 of two telescopes pointing on the same direction of the sky : $\langle E_1 E_2^* \rangle$. For a monochromatic wave in the Fraunhofer limit, the average $\langle E_1 E_2^* \rangle$ is the intensity times a phase factor. The phase factor is given by the geometric path difference between the source and the two telescopes in units of the wavelength. When integrating over the source plane, we obtain the visibility $V(\mathbf{u})$ which is the Fourier Transform of the temperature fluctuation on the sky $\Delta T(\hat{x})$ multiplied by the instrument beam $B(\hat{x})$ [Tompson *et al* (1986)]. The visibility reads

$$V(\mathbf{u}) \propto \int d\hat{x} B(\hat{x}) \Delta T(\hat{x}) e^{2\pi i \mathbf{u}\cdot\hat{x}}$$

where $\hat{x}$ is a unit pointing three-vector, $\mathbf{u}$ is the conjugate variable characterizing the inverse angle measured in wavelength.
The size of the aperture function $A(\hat{x})$ gives the size of the map which means the coverage sky. The maximum spacing determines the resolution. Considering the relatively small field of view of interferometers, we can assume the small-angle approximation and treat the sky as flat. In such conditions, for $u \gtrsim 10$ and $\ell \gtrsim 60$, one can demonstrate that the visibility can be linked to the angular power spectrum as

$$u^2 S(u) \simeq \left. \frac{\ell(\ell+1)}{(2\pi)^2} C_\ell \right|_{\ell=2\pi u}$$

As we have seen, data analysis for interferometers is very specific and we will not go into details in this review. For more complete description, you can refer to [Martin & Partridge (1988)], [Subrahmanyan *et al* (1993)], [Hobson & Mageuijo (1996)], [White (1999)] or [Park *et al* (2003)].

3. Preprocessing

These steps are very instrument dependent. From a general point of view, we transform raw data (figure 13) into a timeline or time-ordered data (TOD). More than just collecting data, this first step often deals with decompression and demodulation data, as well as removing any parasitic signals introduced by, for example, the readout electronics. It may also correct for any non-linear response from the detectors and may flag bad data.

3.1. Demodulation

Data from detectors (scientific signal) and thermometers (housekeeping data) are often modulated in order to provide a method to lockin on the signal. An AC square wave modulated bias, for example, transforms the data into a series of alternative positive and negative values. In the Fourier power spectrum of the data, this induces a peak in the spectrum. This peak dominates the signal and needs to be removed for demodulation. This can be performed by filtering the data with a low-pass filter considering the following constraints:

- the transition after the cut-off frequency must be sharp for complete removal of the modulation signal,

- the ringing of the Fourier representation of the filter above the cut-off frequency needs to be below the approximately 2% level, to avoid aliasing.

The cut-off frequency must be chosen below the Nyquist frequency and above the cut-off due to both the beam pattern and the detector time response in order to preserve the signal.

3.2. Readout electronic noise

When data is stored, it can be compressed into blocks before recording. The data recording can be delayed and a few data blocks are buffered before recording. Small offset variations in the electronics lead to significant differences between the mean value of previously acquired blocks and those following, which induces a parasitic signal on the data. This parasitic signal shows up as periodic pattern in frequency proportional to the ratio of the acquisition frequency over the size of the block, depending on the number of blocks buffered.

3.3. Data flagging

Raw data often contains periods that are suspected or known to be unusable. It can be due to the absence of data or data dominated by parasitic sources such as glitches, noise bursts or jumps due to reconfigurations of the detectors. Those samples are flagged and could be (for some specific purpose such as Fourier transform) filled by constrained realizations of noise. Flagged data are simply not used to make the final CMB maps and power spectra.
Methods to identify these effects are often based on iterative detection of spikes before flagging. At each step, data can be band-pass filtered or convolved with a specific template in order to make the parasitic effect more visible.
Changes in detectors parameters such as the bias produce jumps in the data. Microphonic noise coming from mechanical vibrations or sudden releases of internal mechanical stress can also induce glitches. In addition, bolometers are also sensitive to cosmic ray hits. These are therefore major sources of glitches in bolometer data.
The cosmic ray glitch rate depends on the effective surface of the detector absorber and the observation site (ground, ~ 1 per hour, or balloon/satellite, ~ 1 per minute for a 1mm^2 detector surface). The signature of cosmic-ray hits a delta function convolved with the instrumental response. Thus, collections of cosmic ray responses can be used to estimate the transfer function of the detector and the electronics (see section 6.1). Moreover, a model of energy deposit taking into account the time response of the detectors and electronics gives the shape of the signal as a function of time and helps to estimate how long the data is badly affected by a cosmic ray hit. An approximate model often used is

$$g\left(t, t_i\right) = A \cdot e^{-(t-t_i)/\tau} * f_{em} \; + \; f_{base},$$

where $*$ represents convolution, A is the response amplitude, f_{base} is the baseline, f_{em} is the electronic modulation function and τ is the detector relaxation time constant. Some detectors can show more complex transfer functions with several time constants [Macías-Pérez *et al* (2007), Crill (2001)] that can be related to where the particles deposit their energy on detector.
This process might flag bright sources as cosmic rays. To avoid this, detected glitches are compared with data taken at the same point on the sky at another time with the same or some other detector to confirm that the large signal isn't actually a strong signal on the sky.
Housekeeping data from instrument can also be used to locate and flag specific bad data such as repointing or changes of instrument parameters which can produce jumps.
The main objective is to flag parasitic signal above the noise level. At the end of the process, a small fraction of the data is flagged (usually less than a few percent).

4. Description and subtraction of systematics

In this section we describe systematic effects that can be found in CMB data analysis as well as the methods and algorithms used for their subtraction.

4.1. Description

In a scanning instrument, multipoles of the CMB anisotropies are encoded in time-ordered data at frequencies f which depend on the elevation e and the sky scan speed θ' as

$$f \simeq \frac{\theta'}{2\pi} \cos\left(e\ell\right).$$

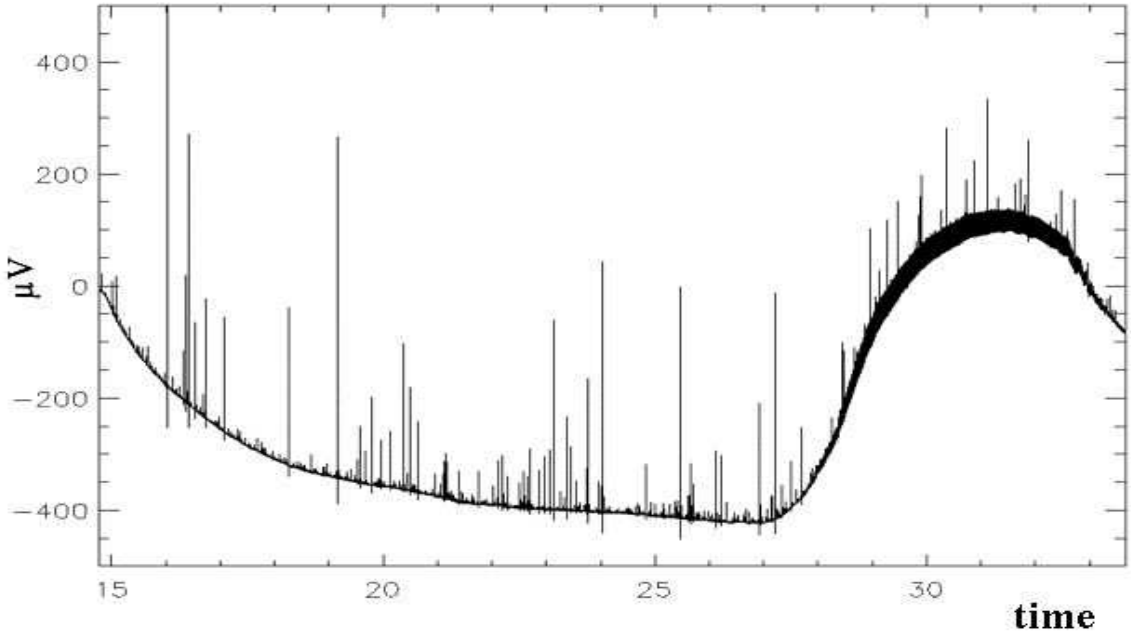

Figure 13. Raw data of Archeops last flight for a bolometer at 143 GHz in arbitrary units. The slow drift is due to a slow change in temperature during the flight. The Sun rose after ∼12 hour of flight. Cosmic rays are clearly visible as spikes in the data.

Depending on the scan strategy, we can define three distinct regimes in the Fourier domain.

- First, the very low frequency components are mainly due to $1/f$-like noise both from detectors (for bolometers) and electronics (both for bolometers and radiometers). Long time-scale drifts from temperature changes of the cryogenic stages and the telescope can also be clearly seen in the time domain. For balloon experiments, drifts can also come from variation of air mass during the flight due to changes in the balloon altitude. Such systematics are highly correlated within detectors and can be monitored by housekeeping data from thermometers and altitude measurements.
- Second, scan-synchroneous systematics are the most difficult to handle. Indeed, at the scan frequency and its harmonics, in addition to the CMB and other extraterrestrial emission, other components can be present experimental contamination can be present.
- Finally the high frequency components are dominated by detector noise. At high frequencies, the Fourier spectrum is nearly flat. For bolometers, time response is closely described by a first order low-pass filter that cuts drastically high frequencies. Microphonic noise can also put imprints on the high frequency noise.

4.2. Subtraction

Systematics that are monitored can be removed via a decorrelation analysis using templates based on housekeeping data and external and/or internal data.
Templates for atmospheric effects can be constructed using altitude and elevation of the payload and a model of the atmosphere, or by using higher frequency detectors which measure at a frequency where atmospheric emission dominates over CMB and other emission. Blind detectors (which are identical to the standard detectors but which have been sealed off from light) are used as microphonic noise monitors. Temperature measurements of different parts of the experiment give us a handle on long-term drift temperature variations.
Correlation coefficients can be computed via linear regression before the templates are subtracted to the data [Masi *et al* (2006), Macías-Pérez *et al* (2007)]. Templates and/or data can be filtered or smoothed depending on the range of frequency of interest.
Although this decorrelation procedure is very efficient, one can often still see correlated low frequency parasitic signals in detectors, which creates stripes in the maps made. To avoid the mixing of the detector signals at this stage of the processing of the data, this effect is usually considered later, when the maps are made.

4.3. Filtering and baseline removing

The easiest way to get rid of long-term drifts, microphonics, or other effects which are localized in Fourier space is simply to apply a highpass, bandpass or a "prewithening" filter.
The purpose of the filter is to clean the data so that the pixel-to-pixel covariance matrix (and thus the noise covariance of the angular power spectrum) becomes simpler. But the filter should modify the underlying signal as little as possible. Thus, noise properties need to be checked after the data treatment and filtering could need iteration.
Data from WMAP radiometers shows some $1/f$ noise at very low frequency (f_{knee} typically of a few mHz [Hinshaw *et al* (2003)]). Even though the effects are small relative to the white noise, it would generate weak stripes of correlated noise along the scan paths. In order to minimize these effect on the final maps, a prewhitening, high-pass filtering procedure has been applied to the data. The method is based on fitting a baseline to the TOD after removal of an estimated sky signal. The baseline is subtracted before the signal is added back in.
For experiments that perform large circles on the sky, the CMB signal in the Fourier domain is located around the scan frequency, so that it is negligible at higher frequencies. A low-pass filter can be used to remove high frequency microphonic noise, while a high-pass filter can be applied to remove very low frequency where $1/f$ noise dominates.

5. Pointing reconstruction

Pointing reconstruction consists of determining for each sample where the detectors are pointing in the sky. The accurate *a posteriori* reconstruction is critical for mapping correctly the sky signal.

5.1. Method

The first step is to reconstruct the pointing direction of the telescope as a whole. This is usually performed using a stellar or solar sensor aligned with the direction of the telescope. This can be combined with several attitude sensors measuring either absolute angles (GPS) or angular velocities (gyroscopes). This step can be described mathematically as a rotational matrix, called the attitude matrix, which converts from an Earth-based reference frame to the telescope frame. It is defined by three Euler angles and so usually described by a quaternion. From stellar sensor data we can reconstruct the pointing direction by comparing observations to catalogs. The sensor outputs can then combined using a Kalman filter [Kalman (1960)], which recursively estimates the state of this dynamic system from a series of incomplete and noisy measurements.
The positions of individual detectors with respect to the telescope can then be reconstructed from measurements of bright, compact sources, such as planets, or bright Galactic or extra-Galactic sources.

5.2. Accuracy

The effect of an unknown, random pointing reconstruction error can be modeled using the modified formula for the uncertainty in a power spectrum mesaurement [Knox (1995)]:

$$\frac{\Delta C_\ell}{C_\ell} = \sqrt{\frac{2}{(2\ell+1)f_{sky}}}\left(1+\frac{w}{C_\ell W_\ell}\right),$$

where w is the noise per beam, f_{sky} is the fraction of the sky covered, and W_ℓ is the transfer function of the beam ($W_\ell = e^{-\ell(\ell+1)\sigma^2}$ for a gaussian beam). The beam causes a loss of sensitivity at higher multipoles ℓ. Pointing uncertainty can be modeled as a smearing of the beam, which increasing the effective beam width. Thus, pointing requirements for CMB experiments are usually fixed by comparison with the level of noise at high multipoles.
As an example, detail on methods for the pointing reconstruction of Planck can be found in [Harrison (2004)].

5.3. Focal plane reconstruction

The position of each photometric pixel in the focal plane relative to the Focal Plane Center is computed using a point source as reference (figure 14). This then allows us to build the pointing of each detector using the pointing reconstruction.

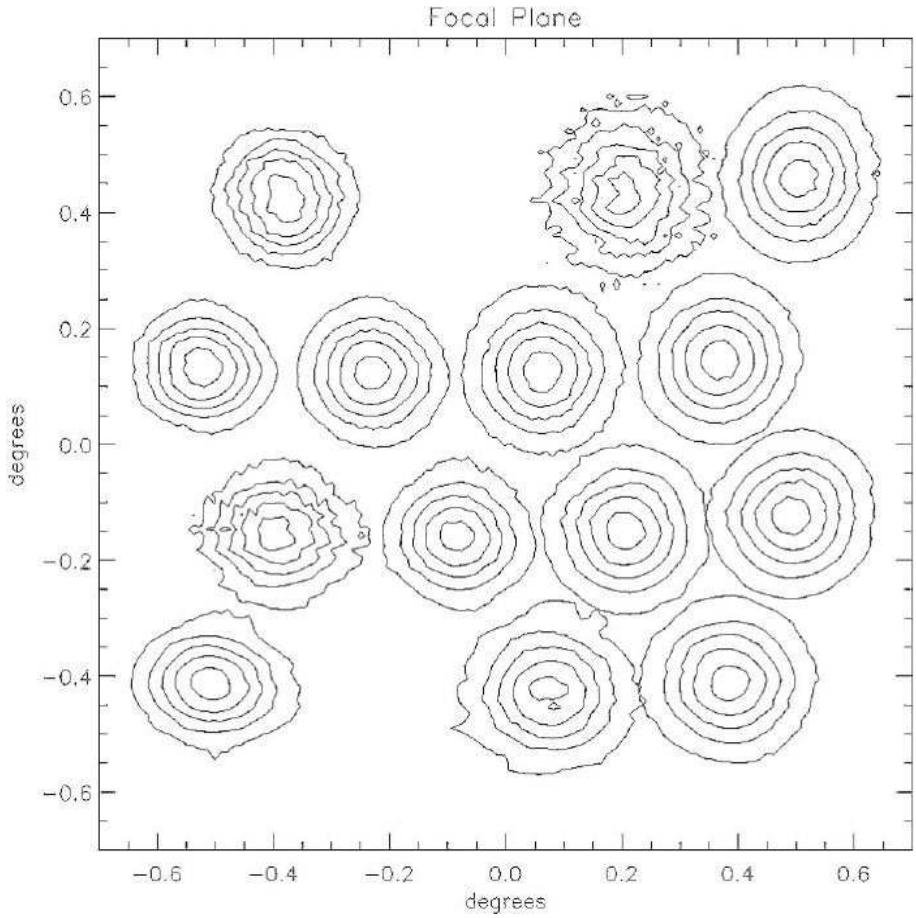

Figure 14. The MAXIMA-II focal plane. The contours, from the center of each beam out, represent the 90%, 70%, 50%, 30%, and 10% levels respectively. (figure extracted from [Rabii *et al* (2006)])

6. Detector response

This section describe the reconstruction of the focal plane parameters: the time response of the detectors, the optical response of the photometric pixels and the focal plane geometry on the celestial sphere.

6.1. Time response

The transfer function of the experiment is usually parameterized by a thermal time constant of the detector and the properties of the readout electronics and filters. The time response of the detectors can often be described by a simple thermal model where the relaxation follows $e^{-t/\tau}$.
The time constant τ can be evaluated on bright sources profiles. Nevertheless, depending on the scanning strategy, it can be difficult to disentangle from, or even degenerate with, the beam shape. This is especially the case for experiments that scan the sky in one direction only, with quasi-constant rotation speed (such as Archeops or Planck), whereas scanning small patches back and forth allows one to deduce the true shape of the beam below the leak due to the time constant (such as for BOOMERanG or MAXIMA).
If an optical method is not usable for some reason, the time response of the detector may also be estimated using the signal from cosmic ray glitches. A cosmic-ray hit on a bolometer is well approximated by a delta function power input. It leaves on the data-stream a typical signature of the response of an impulsive input which correspond to the transfer function of the detector, including electronics. A template of the transfer function can be obtained by piling up all glitches in a given channel after common renormalization both in position and amplitude. It can be either directly used as the detector transfer function (BOOMERanG [Masi *et al* (2006)], figure 15) or used to estimate the parameters of a model (Archeops [Macías-Pérez *et al* (2007)]). For bolometers, due to the internal time constant of the detector absorber, differences can appear with respect to the models. Indeed, the energy deposit on the entire absorber (for millimeter-wave photons) or in a localized area (for cosmic

rays particles) affect differently the response of the detector. In the worst case, several other time constants can appear on glitches, depending on where the cosmic ray hits the detector.

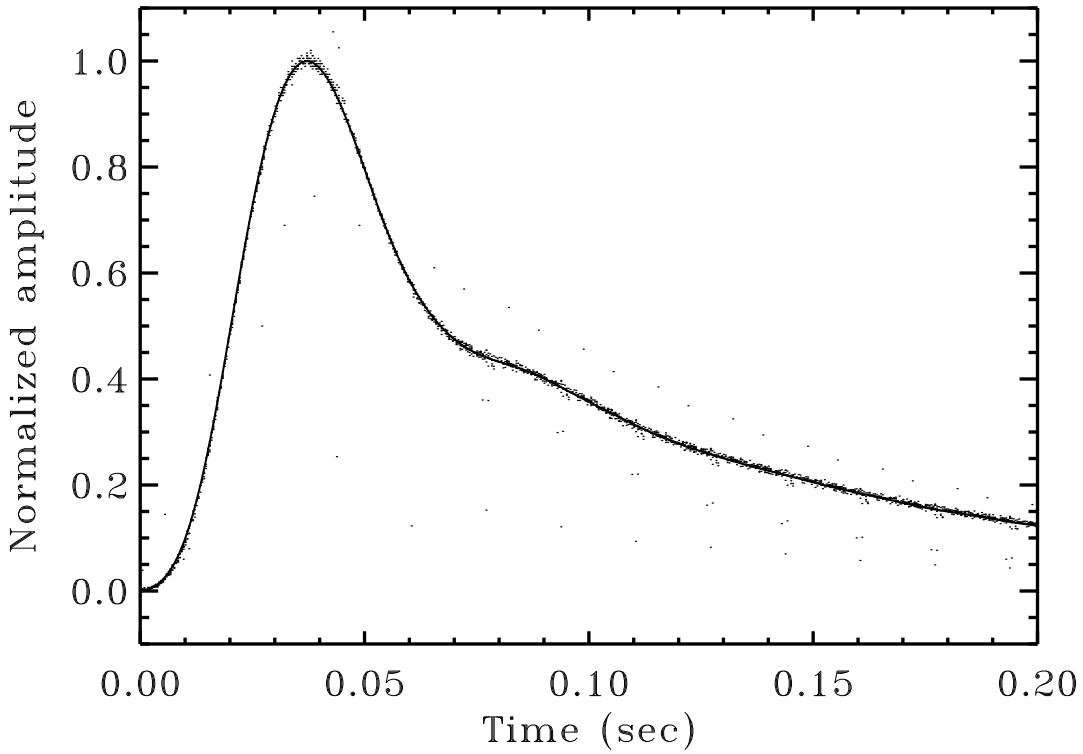

Figure 15. In-flight response of the 145W1 BOOMERanG channel to an impulsive event. The frequency response of the system is the Fourier Transform of this response. The points are accumulated from several cosmic-rays events shifted and normalized to fit the same template. (Figure extracted from [Masi *et al* (2006)])

The result of a time constant is basically to low pass filter a signal. Deconvolving the data stream by the transfer function results in an increase of the noise at higher frequency.

6.2. Beam

The beams represent the optical transfer function of the instrument. The response to point sources for many CMB experiments can often be modeled as a 2D-gaussian, but asymmetry of beams has become one of the most important sources of systematic problems for CMB experiments.
Beams are generally estimated using the response to a point source such as planets or bright stellar objects, which can be combined with physical optics models. For symmetrical beams, a profile in one dimension can be used to ajust the model (BOOMERanG). Otherwise, local maps of brighter sources, such as Jupiter for WMAP [Page *et al* (2003)] or Archeops [Macías-Pérez *et al* (2007)], are constructed to estimate the beam shape.
Multimode horns can show more complex beam pattern with several maxima (for an example, see the Archeops beam pattern [Macías-Pérez *et al* (2007)]).
In CMB analyses, beam effects are often simulated and corrected on the power spectrum rather than deconvoluted in maps domain. Simulations include the convolution by the beam pattern so that the effect is corrected via a transfer function in multipoles (figure 16).
Errors due to an asymmetrical beam pattern being treated as symmetrical a the major source of systematics at high multipoles (figure 17).
Several different methods of modeling beam pattern have been developed. Each observation of the sky is convolved with the beam, which depends both on its shape and on its orientation on the sky. For asymmetric beam patterns, the convolution is then intrinsically linked to the pointing at each point in time, which makes it computationally intensive. Most convolution methods work in harmonic space using either a general convolution algorithm [Wandelt & Hansen (2003)] or a model of the beam pattern

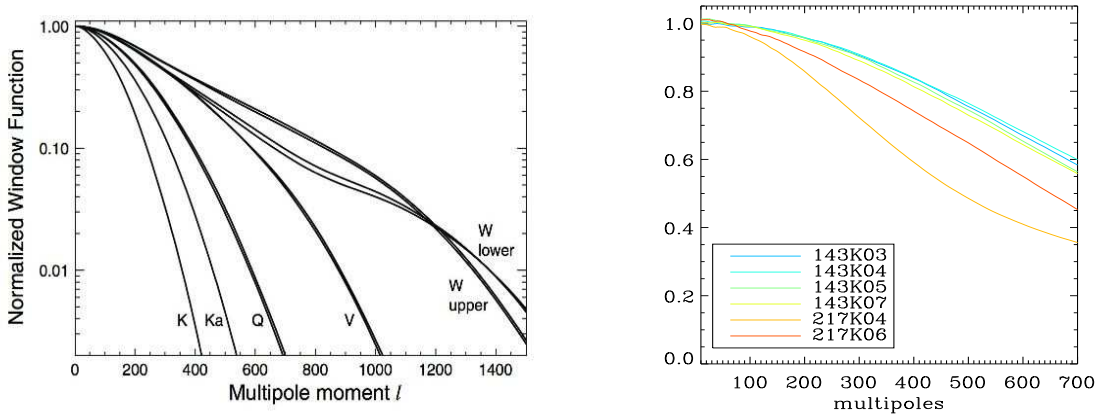

Figure 16. Beam window function in multipole space for a WMAP (*left*, extracted from LAMBDA, http://lambda.gsfc.nasa.gov) detector, and Archeops (*right*, extracted from [Tristram *et al* (2005b)])

in real space that can easily be decomposed in harmonic space. For the latter, several methods have been developed in order to symmetrize the beam [Page *et al* (2003), Wu *et al* (2001)], to approximate the ellipticity [Souradeep & Ratra (2001), Fosalba *et al* (2002)], or decompose the beam pattern into a sum of gaussians [Tristram *et al* (2004)] (BOOMERanG, Archeops).

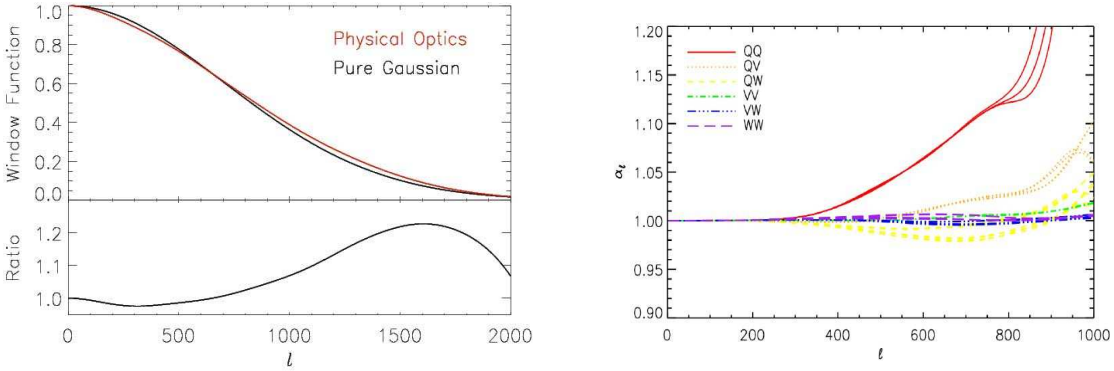

Figure 17. Effects of beam asymmetry on C_ℓ. *Left:* for a BOOMERanG bolometer at 145 GHz, computed from the physical optics model (red line) and a 9.8 arcmin FWHM gaussian beam (black line). (figure extracted from [Masi *et al* (2006)]) *Right:* ratio between the window function for the actual beam and that for a gaussian beam for each WMAP channel. (Figure extracted from [Hinshaw *et al* (2006)])

6.3. Polarization beams

For polarization-sensitive detectors, we define the co- and cross-polarization beams. For a given polarization sensitivity direction at the receiver, the direction of co-polarization at the beam center (on-axis) is conveniently defined as the image of the sensitivity direction through the optics. The cross-polarisation sensitivity direction is orthogonal to the co-polarization.
For data analysis, one needs to estimate the level of cross-polarization in order to characterize the beam patterns and reconstruct the polarized signal of the sky. Moreover, in principle, a significant asymmetry of the main beam can contaminate the polarization measurements.This effect depends largely on the scanning strategy. As for the main intensity beam, the effect of the cross-polarization on the maps is estimated using simulations. For experiments such as WMAP [Jarosik *et al* (2006)] or BOOMERanG [Masi *et al* (2006)], any cross-polarization contribution due to the optics is negligible with respect to the intrinsic cross-polarization of the detectors (figure 18).

6.4. Far sidelobes

In all radio telescopes, each beam has sidelobes, or regions of nonzero gain away from the peak line-of-sight direction. Due to diffraction effects, light from regions of the sky far from the main beam can

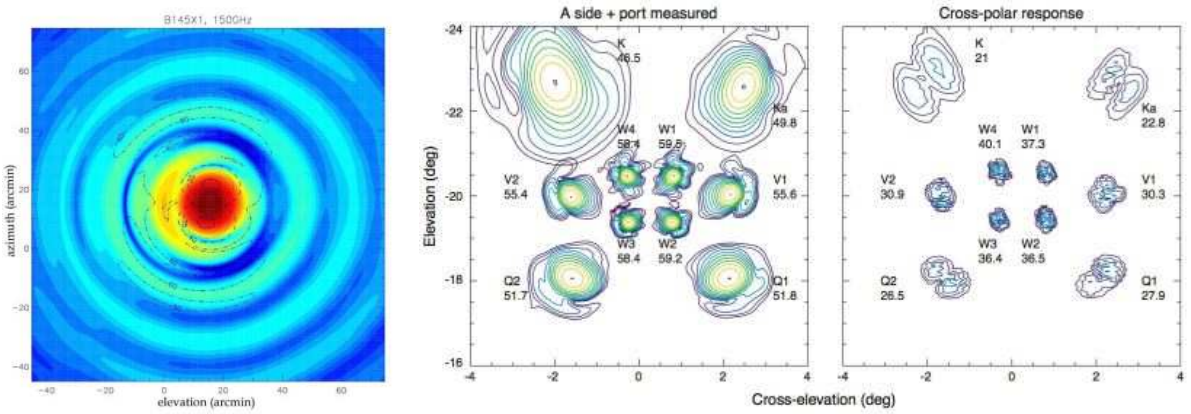

Figure 18. *left:* Comparison of the cross-polar (contours) and co-polar (colors) beams for one of the BOOMERanG 145 GHz channels, as computed with the physical optics code BMAX. (figure extracted from [Masi *et al* (2006)]) *right:* WMAP-measured focal plane for the A side for the co- and cross-polar beams. The contours are spaced by 3 dB and the maximum value of the gain in dBi is given next to selected beams. Measurements at twelve frequencies across each passband are combined using the measured radiometer response. This beam orientation is for an observer sitting on WMAP observing the beams as projected on the sky. (figure extracted from [Jarosik *et al* (2006)])

reach the detectors.
Sidelobe response over 4π sr of sky can be measured from ground-based sources and/or in-flight measurements of very bright sources such as Moon or Sun [Barnes (2003)].
Sidelobe pickup introduces a spurious additive signal into the time-ordered data for each detector. The optical systems of CMB experiments are designed to produce minimal pickup from signals entering the far sidelobes. Thus systematic artifacts remaining in CMB maps can be based on a well-justified assumption that sidelobe effects are small relative to the sky signal.
For most applications in radio astronomy, such weak responses would be negligible. However, the relative brightness of Galactic foregrounds makes side-lobe pickup a potentially significant systematic effect for CMB measurements (3.7% to 0.5% of the total sky sensitivity for WMAP [Page *et al* (2003)]).

7. Calibration

7.1. Spectral calibration

The power absorbed a the detector is a function of the incident optical power, the spectral response and the optical efficiency of the system. The spectral response of the detector is necessary for the analysis of the data. Unlike the calibration gain and offset that can be estimated in-flight, bandpass measurements usually must be made in the lab.
The width of the bands are usually designed to be as broad as possible: $\nu/\Delta\nu \simeq 3$. This gives larger bands at higher frequencies [Jarosik *et al* (2003), Benoît *et al* (2002), Masi *et al* (2006)].

7.2. Gain corrections

The responsivity of CMB detectors depends on the loading they see. This can evolve during the observations. To correct for the gain variation one can make repeated measurements of a known source on the sky (such as the CMB dipole), one can embed a calibration source within the experiment [Crill *et al* (2003)], or one can use a model based on housekeeping data. Gain models are non-linear functions that strongly depend on instrument parameters (for example, detector voltages, gains of amplifiers, phase between radiometers) and monitored temperatures.
After this correction, the calibration factor in mK/μV can be considered as constant over the flight, thus allowing for a much easier determination.

7.3. Absolute calibration

Detectors measure voltage variations that are directly proportional to the temperature variation of the sky. To get back to the temperature, one has to determine a calibration factor by detector. The latter could be considered constant since the time dependance has been subtracted to first order by the linearity corrections above.

Some calibrators that can be used are: the dipole (kinetic and orbital), the galactic diffuse emission and point sources. Usually, for channels dominated by the CMB (between 20 and 300 GHz), calibration on dipole is preferred. Otherwise, at higher and lower frequencies, galactic emission calibration can be successfully applied. Error-bars on point source brightness temperature models and beam model uncertainties makes this kind of calibration usually less precise than those on diffuse emission.

- **Dipoles**
  The Dipole is usually prefered for calibrating experiments with large sky coverage, such as COBE, FIRS, the 19 GHz Experiment, Archeops, WMAP and Planck. This is due to the fact that it depends only marginally on pointing errors, it is a stronger signal than CMB anisotropies by a factor 100, and it has the same electromagnetic spectrum, while not being so bright as to cause non-linearities in the detectors.
  One usually estimates the calibration factor using a linear fit of the time ordered data to a template containing the dipole and galactic emissions. The template is made with measurements made by experiments such as COBE-DMR and WMAP for the kinetic dipole and SFD maps [Schlegel *et al* (1998)] for diffuse galactic emissions.
- **Galaxy**
  In terms of EM-Spectrum coverage and absolute calibration, data from the Far Infrared Absolute Spectrophotometer (FIRAS) instrument on COBE [Mather *et al* (1990)] are the most sensitive. FIRAS products are brightness maps which are converted to photometric maps with the flux convention of constant νI_ν. To be compared with this galactic template, maps from experiments need to be degraded to the FIRAS resolution of $\sim$7 degree.
- **Point sources**
  Point source fluxes (such as from planets) can be compared to brightness models. This calibration method is of particular importance for small coverage experiments that cannot detect the dipole and/or galactic emission with enough signal-to-noise.

7.4. Intercalibration

CMB experiments could have large errors on absolute calibration (due to a small sky coverage for example). But for coadding data from multiple detectors, as well as for polarization measurements, precise intercalibration between detectors is essential. Indeed, the polarization signal from bolometer and radiometer experiments is reconstructed using differences between pairs of detectors. Therefore the accuracy on this reconstruction is very sensitive to the relative calibration. To ensure the precision on intercalibration, one can compare Galactic profiles at constant Galactic longitudes. Relative-calibration factors (usually done on a per-frequency basis) are then obtained by a χ^2 minimization that can be constrained or not via Lagrange multipliers. For polarized detectors, the presence of strongly polarized regions of the sky, especially in the Galactic plane, may affect the determination of the intercalibration coefficients. To avoid this effect, we proceed iteratively and mask, at each step, the strong polarized areas using the projected maps constructed with the intercalibration factors. Attention is paid to build a common mask for all detectors that have to be compared.

8. Data quality checks and noise properties

For further processing of the data, one assumes that the noise is gaussian and piecewise stationary. Statistical tools are used to describe and validate the treatment described above before projecting the data into sky maps. This can be used to check that individual detectors have no strange behavior or inhomogeneous properties.

8.1. Time-frequency analysis

The power distribution of the time-ordered data in the time-frequency (obtained using, for example, wavelets tools) can be used to find special features in the noise in time limited domains. These features can be due to differences in the foregrounds signal for particular scanning strategies at low frequencies together with $1/f$ noise of detectors. After systematic subtraction, the power distribution should be flat.
Time-frequency analysis, such as in [Macías-Pérez & Bourrachot (2006)], allows us to exclude from the further processing the detectors which present either strong or highly time variable systematic residuals.

8.2. Noise power spectrum estimation

Estimation of the Fourier power spectrum of the noise is essential in CMB analysis. First, it can be used to fill the small gaps in the data such as those due glitches or point sources subtraction, for specific analyses and second, we need an accurate estimate of it for Monte-Carlo purposes.
Gap filling is necessary for map making process and Fourier power spectrum estimations that requires continuous data (for example, if we want to use the fast fourier transform). Gaps are filled with what we call locally constrained realizations of noise. Simple algorithms are based on a reconstruction of low and high frequency components separately. First, we reconstruct the low frequency noise contribution via an interpolation within the gap using an irregularly sampled Fourier series. Finally, we compute the noise power spectrum locally (in time intervals around the gap) at high frequency and we produce a random realization of this spectrum. Notice that we are only interested in keeping the global spectral properties of the data. Moreover, the gaps are in general very small in time compared to the piece of the data used for estimating the power spectrum, and therefore this simple approach is usually accurate enough.
Both Maximum Likelihood map making and angular power spectrum estimation can heavily depend on the knowledge of the noise spectral density. Bayesian approaches can be used in order to estimate the noise [Natoli *et al* (2002)] or simultaneously the noise and the signal [Ferreira & Jaffe (2000)] in the data. Considering the low signal-to-noise ratio in CMB data, a first estimate of the noise power spectrum can be directly derived from the data themselves. Then, we can iterate to higher precision. We found algorithms that rely on the iterative reconstruction of the noise by subtracting from the TOD an estimate of the sky signal [Amblard & Hamilton (2004)] useful. This latter is obtained from a coadded map which at each iteration is improved by taking into account the noise contribution.

8.3. Gaussianity of the noise

To this point, we have only considered the power spectrum evolution to define the level of stationarity of the data. To be complete in our analysis we first have to characterize the Gaussianity of the noise distribution and second check its time stability.
Kolmogorov-Smirnov tests can be used to check the time evolution of the noise of each detector. The Kolmogorov-Smirnov significance coefficient gives the confidence level at which the hypothesis that the noise has been randomly drawn from a Gaussian distribution can be accepted. As intrinsic detector noise can usually be considered Gaussian to a very good approximation, any changes in the distribution function of the noise will indicate the presence of significant deviations from systematics such as Galactic and/or atmospheric signals, which are neither Gaussian nor stationary.
[Macías-Pérez *et al* (2007)] use a Kolmogorov-Smirnov test in the Fourier domain. Working in the Fourier domain both speeds up the calculations and isolates the noise, which dominates at intermediate and high frequencies, from other contributions like the Galactic and/or atmospheric signals at low frequency. Then, Kolmogorov-Smirnov statistics under the hypothesis of a uniform distribution is applied in consecutive time intervals, which are compared two by two.

9. Map making

Once the data has been "cleaned", the time-ordered samples must be be projected onto a pixelized map of the sky using the associated pointing information. To each measurement in time is associated a pixel in its pointing direction.
The most common pixelization scheme used in CMB data analysis today is the Hierarchical Equal Area isoLatitude Pixelization, or HEALPix‡ [Gorski *et al* (2005)], in which each pixel is exactly equal-area, and in which pixels lay on sets of rings at constant latitude. This allows one to take advantage of fast Fourier transforms in the analysis, when decomposing the map data into spherical harmonics [Muciaccia *et al* (1997)].
If the experiment has sensitivity to polarization, given the orientations of the detectors on the sky as a function of time, maps of the Q and U stokes parameters are also reconstructed from the signal.

9.1. The Map-making problem

Our detectors measure the temperature of the sky in a given direction through an instrumental beam. This is equivalent to saying that the underlying sky is convolved with this instrumental beam. The

‡ http://healpix.jpl.nasa.gov

time-ordered data vector, $\mathbf{d}$, may therefore be modeled as the sum of the signal from the pixellized, convolved sky $\mathbf{T}$ and from the noise $\mathbf{n}$:

$$\mathbf{d} = \mathbf{A} \cdot \mathbf{T} + \mathbf{n}.$$

The pointing matrix A, of size $N_t \times N_p$, relates each time sample to the corresponding pixel in the sky. For detectors not sensitive to polarization, T_p is the temperature of the sky in the pixel p and each element of A is a scalar. For polarized-sensitive detectors, $T_p = (I, Q, U)_p$ also contains the Stokes parameter values in the pixel p, so each element of the matrix A is a 3×3 matrix such that

$$d_t = I_p + Q_p cos(2\psi_t) + U_p sin(2\psi_t) + n_t,$$

where ψ_t is the angle of the detector's polarization direction, with respect to the polarization basis in the pixel p, at the time t.

Defined so, A is very sparse. For an ideal optimal beam, it contains only one (three for polarization-sensitive detectors) non-null values in each row, as each time sample is sensitive to only one pixel of the convolved sky. For an axisymmetric beam response, the "smearing" and "pointing" operations commute, and one can solve for the beam convolved map. However, this is not exact for an asymmetric beam because the latter couples to the scanning strategy. In that case, we can use more specific method to perform the deconvolution of the beam [Arnau & Saez (2000), Burigana & Sáez (2003), Armitage & Wandelt (2004)].

At this point, it is usually assumed that the noise properties are Gaussian and piece-wise stationary (if not, more filtering and data cleaning are usually done). Both assumptions are crucial, as they allow major simplifications of the map-making and power spectrum estimation problems. Namely, Gaussianity means that all the statistical information of the noise is contained in its covariance matrix $\mathbf{N}$. That is,

$$N = \left\langle \mathbf{n}\mathbf{n}^T \right\rangle,$$

where the symbols $\langle\ \rangle$ indicate an ensemble average.

Using the stationarity assumption, the noise can also be described by its Fourier power spectrum, leading to major simplifications of the covariance matrix. It implies that each stationary block of N is a symmetric Toeplitz matrix [Golub & van Loan (1996)], diagonal in the Fourier space.

Given the above, the map-making problem becomes that of finding the best estimate, $\hat{\mathbf{T}}$, of the sky, $\mathbf{T}$, given our data, $\mathbf{d}$, and scanning strategy, $\mathbf{A}$ [Stompor *et al* (2002)].

9.2. A simple solution : "coaddition"

If the noise in the time-ordered data is "white", then we can make maps in the most intuitive manner – simply by binning data into pixels on the sky. This is what we call "coaddition".

$$\hat{\mathbf{T}} = \left[\mathbf{A}^T\mathbf{A}\right]^{-1}\mathbf{A}^T\mathbf{d}. \tag{9.1}$$

The operator $\mathbf{A}^T$ sums the time-ordered data into the correct sky pixel, while $\mathbf{A}^T\mathbf{A}$ is a diagonal matrix, with the value of each diagonal element being the number of time-ordered samples which have fallen into the corresponding pixel – it gives the number of samples binned into each pixel. If the noise in each data sample is independent, that is if the noise is white, the constructed map is optimal in terms of signal to noise ratio.

Often, however, the noise in our measurements is correlated, resulting in pixel-to-pixel correlations in maps. Since much of the science of the CMB depends on measuring correlations between different points on the sky, it is necessary to characterize and account for these correlations, which complicates our map making procedures somewhat.

9.3. Maximum Likelihood (ML) methods

The most general solution to the map-making problem is obtained by maximizing the likelihood of the data given a noise model [Wright (1996), Tegmark (1997)]. As the noise is Gaussian and assuming a uniform prior on the sky temperature, the likelihood reads

$$P(\mathbf{T}|\mathbf{d}) \propto \frac{1}{\left|(2\pi)^{N_t}N\right|^{1/2}} e^{-(\mathbf{d}-\mathbf{A}\mathbf{T})^T\mathbf{N}^{-1}(\mathbf{d}-\mathbf{A}\cdot\mathbf{T})/2}$$

Maximizing this equation with respect to each pixel of $\mathbf{T}$ leads to the generalized least-squares (GLS) equation

$$\mathbf{A}^\dagger\mathbf{N}^{-1}\mathbf{A}\hat{\mathbf{T}} = \mathbf{A}^\dagger\mathbf{N}^{-1}\mathbf{d}. \tag{9.2}$$

The solution to this is, of course

$$\hat{\mathbf{T}} = \left(\mathbf{A}^T\mathbf{N}^{-1}\mathbf{A}\right)^{-1} \cdot \mathbf{A}^T\mathbf{N}^{-1}\mathbf{d}.$$

Note that $\hat{\mathbf{T}}$ is also the minimum variance estimate of the map for gaussian noise. If the noise is not Gaussian, the GLS estimator still has the minimum variance among all linear estimators. Also, if the noise in the time-ordered data is white, $\mathbf{N}$ is diagonal and this solution is the same as the "coadded" map solution given in equation 9.1.
The covariance matrix of the resulting map is

$$\mathcal{N} = \left(\mathbf{A}^T \cdot \mathbf{N}^{-1} \cdot \mathbf{A}\right)^{-1}.$$

A couple of points:

- ML map-making methods usually consider noise correlations on smaller subsets of the data [Natoli *et al* (2001)]. In this case, the matrix $\mathbf{N}$ becomes circulant and the product $\mathbf{N}^{-1}\mathbf{d}$ can be computed in the frequency domain in which $\mathbf{N}^{-1}$ is diagonal.
- In practice, the inversion or even the convenient calculation of the $N_p \times N_p$ matrix $\mathbf{A}^T\mathbf{N}^{-1}\mathbf{A}$ is impossible for large datasets such as Archeops, WMAP or Planck. Thus, equation 9.2 is usually solved using methods such as the preconditioned conjugate gradient (PCG) [Golub & van Loan (1996)] or FFT methods. Iterations are repeated until the fractional difference between successive iterations has reached a low enough value (typically of the order of 10^{-6}).

Among the codes that have been developed to solve the generalized least squares (GLS) mapmaking equation using iterative conjugate gradient descent and FFT techniques, most have already been applied successfully to CMB data sets. MapCUMBA [Doré *et al* (2001)] has been used to construct the Archeops and BOOMERanG maps. Mirage [Yvon & Mayet (2005)] has been successfully applied to Archeops data. ROMA [de Gasperis *et al* (2005)] has also been used to analize data from the last (2003) Antarctic flight of BOOMERanG. These codes with MADmap [Borrill (2007)] have been extensively compared in the Planck framework [Ashdown *et al* (2006b)].

9.4. Destriping methods

So-called "destripers" attempt to simplify the general map making problem described above when the solutions above would require too many resources. An early, basic destriper was developed for the 19 GHz experiment [Boughn *et al* (1992)].
It has been shown [Janssen *et al* (1996)] that instrumental noise, in particular $1/f$ noise, can be represented by an uniform offset on a scan circle signal. In the destriping approach, the noise is divided into a low-frequency component represented by the offsets $\mathbf{x}$ unfolded on time-ordered data by the matrix $\mathbf{\Gamma}$ and a white noise part $\mathbf{n}$ which is uncorrelated

$$\mathbf{d} = \mathbf{A} \cdot \mathbf{T} + \mathbf{\Gamma} \cdot \mathbf{x} + \mathbf{n}$$

The maximum-likelihood coefficients, $\mathbf{x}$, can be found from the time-ordered data, $\mathbf{d}$, by solving

$$\left(\mathbf{\Gamma}^T\mathbf{N}^{-1}\mathbf{Z}\mathbf{\Gamma}\right) \cdot \mathbf{x} = \mathbf{\Gamma}^T\mathbf{N}^{-1}\mathbf{Z} \cdot \mathbf{d}$$

where

$$\mathbf{Z} = \mathbf{I} - \mathbf{A}\left(\mathbf{A}^T\mathbf{N}^{-1}\mathbf{A}\right)^{-1} \cdot \mathbf{A}^T\mathbf{N}^{-1}.$$

The destriping technique for the CMB map-making has been investigated in minute detail for the Planck satellite [Burigana *et al* (1997), Delabrouille *et al* (1998), Maino *et al* (1999), Maino *et al* (2002a), Keihanen *et al* (2004)], which we will follow here. It exploits the fact that Planck is spinning and thus detectors observe large circles on the sky over and over, with each circle being observed several times (of order 60). Averaging over these circle makes rings with higher signal-to-noise ratio. To extract the values of the offsets, detripers use the redundancy of the observing strategy by considering the intersections between rings. Intersections are defined when two points from different scan circles fall inside the same sky pixel.
After the amplitudes of the offsets have been estimated, they can be used to extract an estimate of the $1/f$ noise component in the data. A "cleaned" map is then obtained by simply coadding rings. Residuals of $1/f$ noise found in the clean map for a knee frequency below 0.4 Hz have been shown significantly below the noise level [Maino *et al* (2002a)] considering a Planck-like scanning strategy (figure 19).

Destriper codes have been developed in the context of Planck analysis : Polar [Keihanen *et al* (2007)], MADAM [Keihanen *et al* (2005)], Springtide [Ashdown *et al* (2006a)] and Polkapix [Perdereau *et al* (2007)]. In fact, as shown in [Poutanen *et al* (2006)] and [Ashdown *et al* (2006b)], the baseline length used need not be tied to the length of a Planck ring; thus the codes above are generalizations of the Janssen presciption. Including priors on the low frequency noise, the destriping algorithm is equivalent to the GLS algorithm in the short baseline limit. Similarly, GLS "optimal" codes can be considered as destripers with a baseline fixed by the detector sampling rate and an accurate description of the noise covariance properties.

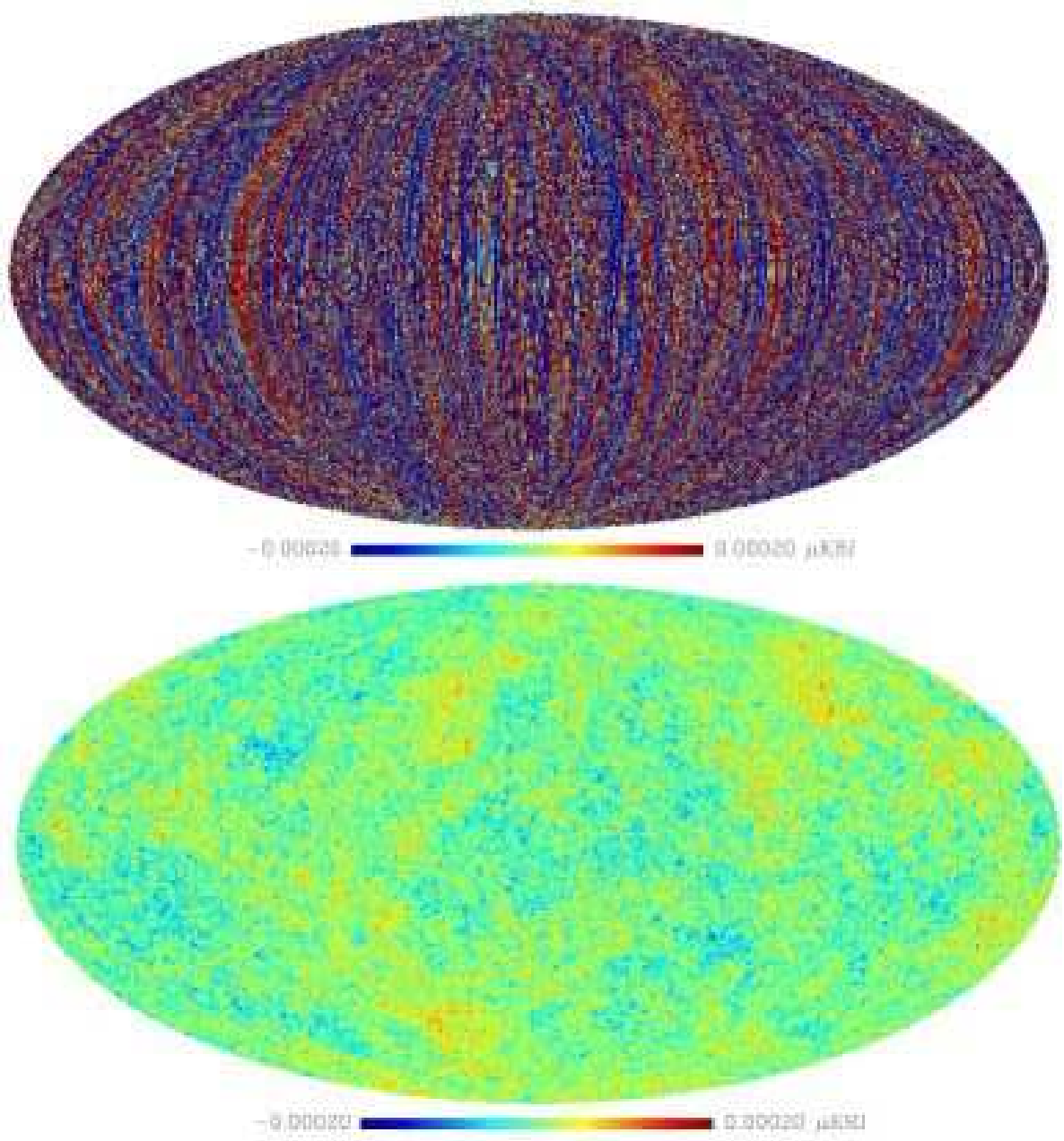

Figure 19. Simulation at 217 GHz for Planck before (*top*) and after destriping (*bottom*). Simulations only include $1/f$ noise and CMB signal.

10. Foreground removal

Maps obtained from CMB data measure the temperature variation of the sky including astrophysical components in addition to the signal of the CMB. The primary goal for a CMB experiment is to remove the foregrounds to provide a clean map of the CMB for cosmological analysis. But this process can also improve understanding of foreground astrophysics.

Removal methods typically rely on the fact that the foreground signals have quite different spatial and spectral distributions than the CMB. Galactic free-free and synchrotron emissions decrease in amplitude with frequency whereas Galactic dust and atmospheric emission rise (figure 6). Thus, lower and higher frequency channels are most sensitive to free-free and synchrotron or dust and atmospheric emission, respectively.

10.1. Linear combination

Multi-frequency sky maps can be linearly combined to subtract, to first order, Galactic signals, while preserving the CMB. Calibration factors and systematic effects can alter this combination when using different data sets.
The most simple way to obtain a clean CMB map is to minimize the variance of the resulting map, constraining the sum of the coefficients in order to preserve the CMB signal [Bennett *et al* (2003b)]. [Eriksen *et al* (2004a)] developed a similar method considerably faster by using a Lagrange multiplier to linearize the problem. The method is template-free and can be efficient but gives a single CMB map with complicated noise properties.

10.2. Template removal

Decorrelation algorithms use templates of these emissions to subtract parasitic signals either in the map or in the time domain. Templates are constructed from observations, coming either from the same experiment or not, and extrapolated in frequency.
Galactic signals dominate at low frequencies in time domain (less than a few Hz). Templates can be bandpass filtered in that range in order to improve the efficiency of these algorithms. The correlation coefficients are then directly computed via a simple regression analysis. A linear combination of the templates multiplied by the correlation coefficients is then removed from the data.
Extrapolation in frequency and in space can give non-negligible residuals in the decorrelated maps. It is thus important to estimate the residual foreground uncertainties that remain after these templates have been fit and subtracted. Nevertheless, template-based maps have been used for the CMB anisotropy power spectra estimation of WMAP [Hinshaw *et al* (2006)], Archeops [Macías-Pérez *et al* (2007)] and BOOMERanG [Masi *et al* (2006)].

10.3. Component separation

Component separation algorithms take advantage of the fact that CMB and foregrounds have different EM-spectra.
The signal from several channels at different frequencies can be modeled as a linear combination of astrophysical components plus noise. This leads to a decomposed representation of:

$$x^d_{\ell m} = A_{dc}\ s^c_{\ell m} + n^d_{\ell m},$$

where the data $x^d_{\ell m}$ are decomposed into spherical harmonic coefficient by detector d. The mixing matrix A_{dc} describes the amplitudes of each of the components c for each detector d. $s^c_{\ell m}$ and $n^d_{\ell m}$ are the spectra of the components and of the noise, respectively. Coefficients of the mixing matrix A are linked to the electromagnetic spectrum of each component and to the relative calibration between detectors.
Maximum likelihood methods give a simple solution of the problem in the case where we have stationary gaussian noise characterized by its auto-correlation matrix N:

$$\tilde{s} = \left(A^t N^{-1} A\right)^{-1} A^t N^{-1} y.$$

More sophisticated algorithms have been developed:

Wiener solutions [Bouchet & Gispert (1999), Bouchet *et al* (1999)]. The Statistics of the astrophysical components must be gaussian and stationary and their spectrum is assumed to be known. The likelihood function includes a term that take into account the correlation of s in spherical harmonic space.

Maximum entropy [Hobson & Lasenby (1998)]. In contrast to the Wiener solution, this does not assume Gaussianity of the components, but still requires us to know A and N. Prior assumptions on components are taken into account through a additional term in the likelihood that contains the entropy of the system.

Independent Component Analysis (ICA) [Maino *et al* (2002b), Baccigalupi *et al* (2004), Aumont & Macías-Pérez (2007)]. These algorithms do not assume any priors on components. They compute the deviations with respect to a model of gaussian components equally distributed. This differences can result in non-gaussian effects, non-stationary effects and spectral dependancy effects [Delabrouille *et al* (2003)].

11. Angular Power Spectrum Estimation

The angular power spectrum of CMB anisotropies has become one of the most important tools of the modern cosmology. While in the linear regime, fluctuations predicted by most inflationary models [Hu *et al* (1997), Linde *et al* (1999), Liddle & Lyth (2000)] result in gaussian anisotropies. In such cases, angular power spectra both in temperature and polarization contain all the cosmological information in the CMB. In particular, cosmological parameters can be derived from these spectra.
In the last decade, CMB data have grown considerably in both quantity and quality. Concurrently, methods have been developed to estimate the angular power spectra from maps as quickly as possible. This has allowed direct comparisons of theoretical predictions and observations using fast and accurate statistical methods. Moreover, great efforts have been made on simplifying angular spectra estimators so that they can deal with the huge amount of accurate data in a reasonable amount of time, especially in light of the new arrays of detectors that will soon multiply the number of detectors by one or two order of magnitude.
Except for very specific methods that, for example, estimate spectra on rings for Planck-like scanning strategies [van Leeuwen *et al* (2002), Challinor *et al* (2002), Ansari *et al* (2003)], most power spectra estimators belong to one of the two following categories: maximum likelihood algorithms or quadratic estimators usually called *pseudo*-estimators (see [Efstathiou (2004)] and [Efstathiou (2006)] for a complete discussion).
Maps of I, Q and U components of the CMB signal are decomposed into spherical harmonics $a^T_{\ell m}$, $a^E_{\ell m}$ and $a^B_{\ell m}$. From these coefficients, one can construct the 6 angular power spectrum : C^{TT}_ℓ, C^{EE}_ℓ, C^{BB}_ℓ, C^{TE}_ℓ, C^{TB}_ℓ and C^{EB}_ℓ. Systematic effects need to be taken into account in this process. In particular, beam smoothing effects or partial coverage of the sky must be accounted for. Even for full sky missions, foreground residuals usually still dominate the noise in the Galactic plane. To avoid any contamination of the angular power spectra, a mask is applied to suppress pixels of the sky dominated by parasitic signal, leading to less than full-sky effective coverage.

11.1. Maximum Likelihood methods

Maximum likelihood algorithms [Bond *et al* (1998), Tegmark (1997), Borrill (1999a)] estimate angular power spectra using the angular correlation function M by maximizing the probability of C_ℓ considering the maps T:

$$\mathcal{P}(C_\ell|T) \propto \exp\left[-\frac{1}{2}\left(T^T M^{-1} T + Tr(\ln M)\right)\right].$$

The correlation matrix of pixels M includes the correlations between pixels due to sky signal, S, and that due to noise N: $M_{pp'} = S_{pp'} + N_{pp'}$. Thus, the signal correlation matrix reads

$$S_{pp'} = \sum_\ell \frac{2\ell+1}{4\pi} B^2_\ell C_\ell P_\ell\left(\cos\theta_{pp'}\right)$$

where $\theta_{pp'}$ is the angle on the sphere between pixels p and p'.
Error bars are usually estimated directly from the likelihood function which is either sampled for each multipole or approximated by a quadratic form. The generalization to polarization can be found in [Tegmark & de Oliveira-Costa (2001)].
The algorithm scales as $\mathcal{O}\left(N^3_{pix}\right)$ where N_{pix} is the number of pixels in the map. This implies that maximum likelihood methods are not well adapted to surveys such as Planck which should deliver high resolution maps with more than 10^7 pixels [Borrill (1999b)].

11.2. Quadratic estimator or pseudo-C_ℓ methods

Contrary to maximum likelihood algorithms, *pseudo-*C_ℓ methods compute the angular power spectra directly from the data. These spectra are biased by instrumental effects such as beam smoothing effects, partial sky coverage or filtering of data and so must be corrected for these effects. Methods differ in the way they correct spectra for these effects.

An early description of this method can be found in [Peebles (1973)], and has been used for the estimation of the angular power spectrum of clusters of Galaxies [Peebles & Hauser (1974)]. More recently, several methods have been developed, among them:

- SPICE [Szapudi *et al* (2001)] and its extension to polarization [Chon *et al* (2004)]:
  This algorithm computes the two-point correlation function ξ in real space in order to correct for any inhomogeneous sky coverage and then integrate with a Gauss-Legendre quadrature to obtain the C_ℓ's.
  The method uses the correlated function estimator given by

$$D(cos\theta) = \sum_{lm} |a_{lm}|^2 \frac{1}{4\pi} P_\ell(cos\theta)$$

  The unbiased correlation function estimator can thus be obtained as

$$\tilde{\xi}(cos\theta) = \frac{D_s(cos\theta) - \bar{D}_n(cos\theta)}{D_w(cos\theta)}$$

  where D_s is the raw weighted pairwise estimator, $\bar{D}_n$ is the average raw noise correlation function calculated from Monte-Carlo simulations and D_w is the weight correlation function.
- MASTER [Wandelt *et al* (2001), Hivon *et al* (2002)]:
  This algorithm computes the angular power spectra directly from the observed maps before correcting for the inhomogeneous sky coverage in spherical harmonic space. An extension to polarization can be found in [Hansen & Górski (2003), Challinor & Chon (2005), Brown *et al* (2005)]. The biased spectrum (called pseudo-spectrum) $\widetilde{C}_\ell$ rendered by the direct spherical harmonics transform of a partial sky map is different from the full sky angular spectrum C_ℓ but their ensemble average are linked by :

$$\langle \tilde{C_\ell} \rangle = \sum_{\ell'} M_{\ell\ell'} F_{\ell'} B^2_{\ell'} \langle C_{\ell'} \rangle + \langle \tilde{N_\ell} \rangle.$$

  $M_{\ell\ell'}$, which is computed analytically using the spherical transform of the weight mask, describes the mode-mode coupling resulting from the cut sky. B_ℓ is a window function describing the combined smoothing effects of the beam and finite pixel size. $\langle \tilde{N_\ell} \rangle$ is the average noise power spectrum estimated by Monte-Carlo. F_ℓ is a transfer function which models the effect of the filtering applied to the data stream or to the maps.

Pseudo-C_ℓ estimators often make use of the fast spherical harmonics transform that scales in $\mathcal{O}\left(N_{pix}^{3/2}\right)$ for the HEALPix pixelization scheme [Gorski *et al* (2005)]. Nevertheless, they need a precise description of the instrument (beam, filtering, noise) that requires a large number of Monte-Carlos. These latter are also used to estimate the power spectrum error bars.
Recently, these methods have evolved into cross-correlation methods that deal naturally with uncorrelated noise [Kogut *et al* (2003)], and can compute analytical estimates of the error bars [Tristram *et al* (2005a)]. A cross-correlation method derived from the MASTER algorithm has been used to estimate the lastest results of WMAP [Hinshaw *et al* (2003)], Archeops [Tristram *et al* (2005b)] and BOOMERanG [Jones *et al* (2006), Montroy *et al* (2006), Piacentini *et al* (2006)].

11.3. Hybrid methods

Each of the previous methods make different assumptions about the data and are sensitive to different kinds of systematic effects. [Efstathiou (2004)] and [Efstathiou (2006)] show how to combine maximum likelihood methods and pseudo-C_ℓ methods to take advantage of both algorithms.

- **high ℓ.** pseudo-C_ℓ methods, including cross-correlation algorithms, can estimate the C_ℓ quickly and accurately enough when instrumental noise is dominant; *i.e.* at higher multipoles. Nevertheless, approximations made in the correlation matrix computation imply some correlation for the lower points of the spectra.
- **low ℓ.** Maximum likelihood algorithms used on lower resolution maps can give very precise estimates of the spectra at low multipoles as well as error bars and covariance matrices. Nevertheless, they are very CPU consuming and are not adapted to high resolution maps.

11.4. Fourier spectrum of rings Γ_m

Several CMB experiments have performed or will perform circular scans on the sky which we will call *rings* (the 19 GHz experiment, FIRS, Archeops, WMAP, Planck). Carrying out a one-dimensional analysis of the CMB inhomogeneities on rings provides an alternative to characterize its statistical properties [Delabrouille *et al* (1998)]. In particular, some systematic effects could be easier to treat in the time domain rather than in the two-dimensional maps; $1/f$ noise for instance.
In [Ansari *et al* (2003)], the authors propose a scaling law that allows one to combine spectra corresponding to different colatitude angles (e.g. several detectors in the focal plane) before to inverting to recover the angular power spectrum C_ℓ.

11.5. Gibbs samplers

Gibbs sampling [Jewell *et al* (2004), Wandelt *et al* (2004)] allows one to sample the power spectrum directly from the joint likelihood distribution given the time ordered data. While maximum likelihood methods define an estimator to solve the *a posteriori* density, Gibbs sampling methods for power spectrum estimation [Eriksen *et al* (2004b)] propose sampling parameters values C_ℓ from the posterior $P(C_\ell|m)$ directly (where the map vector m is the least squares estimate of the signal s from the time ordered data). The method works iteratively by sampling the conditional distributions $P(s|C_\ell, m)$ and $P(C_\ell|s, m) \propto P(C_\ell|s)$ [Tanner (1996)]. Each step is obtained from the previous one, drawing a random realization from each density:

$$s^{i+1} \leftarrow P(s|C_\ell^i, m)$$
$$C_\ell^{i+1} \leftarrow P(C_\ell|s^{i+1})$$

After convergence, $P(C_\ell|m)$ is obtained by marginalization of $P(C_\ell, s|m)$ over s.
The linear systems are solved using a conjugate gradient algorithm. The choice of a good preconditioner for the linear algebra solver is of primary importance. Nevertheless, the calculations are dominated by the spherical harmonic transforms that scales in $\mathcal{O}(N_{pix}^{3/2})$. It has been applied to both COBE-DMR data [Wandelt *et al* (2004)] and WMAP first-year [O'Dwyer *et al* (2004)].

12. Analysis of distribution of CMB anisotropies

A consequence of the assumed flatness of the inflation potential is that intrinsic non-linear effects during slow-roll inflation are generally quite small, though finite and calculable [Acquaviva *et al* (2003), Maldacena (2003)]. The adiabatic perturbations arising from quantum fluctuations of the inflaton field during inflation are thus essentially Gaussian distributed. However, the mechanism by which the adiabatic perturbations are generated is not fully established. Some alternative scenarios (such as the curvaton or inhomogeneous reheating mechanisms) can lead to a higher levels of non-gaussianity than that found in standard, single-field inflation. Moreover, variants of the most simple inflationary models also predict observable levels of non-gaussianity (e.g., generalised multi-field models [Wands *et al* (2002)], cosmic defects [Landriau & Shellard (2003)] or late time phase transition). Thus, to give a completely validate the inflationary fluctuation generation mechanism, it is important to study the distribution of phases in temperature and polarization maps and quantify the amount of primordial non-Gaussianity present in the CMB data. If found, a more accurate description of this non-gausianities will be needed to distinguish between competing models for primordial perturbation generation. In addition, the search for non-Gaussianities has become a powerful tool to detect the presence of residual foregrounds, secondary anisotropies (such as gravitational lensing, Sunyaev-Zel'dovich effect) and unidentified systematic errors, which leave clearly non-Gaussian imprints on the CMB-anisotropies data.
There are many techniques to test Gaussianity, many of them developed previously as general statistical methods to test the normality of a data set, and others specifically for CMB anisotropies. Most early works tested only the consistency between CMB maps and simulated Gaussian realizations. More recent studies now derive constraints on a parameter, f_{NL}, characterizing the amplitude of the primordial non-Gaussianity in the primordial gravitational potential Φ, characterized as a linear gaussian term plus a quadratic contribution

$$\Phi(\mathbf{x}) = \Phi_G(\mathbf{x}) + f_{NL}\Phi_G^2(\mathbf{x})$$

Among methods applied to CMB datasets we highlight:

- one-point moments, such as skewness and kurtosis;
- bispectrum analyses based on the Fourier Transform of the three-point correlation function;

- geometrical estimators on the sphere;
- Minkowski functionals;
- goodness-of-fit tests;
- wavelet decompositions; and
- steerable filters to search for aligned structures;

Instrumental effects and observational constraints are usually taken into account through Monte-Carlo simulations to estimate distributions of the testing statistic and the confidence levels.
To date there is no evidence for significant cosmological non-Gaussianity. Several groups have claimed detections of significant non-Gaussianities in the first-year WMAP sky maps [Tegmark *et al* (2003), Eriksen *et al* (2004c), Copi *et al* (2004), Vielva *et al* (2004), Hansen *et al* (2004), Park (2004), Cruz *et al* (2005)]. However, the WMAP team has shown that most of these detections are based on *a posteriori* statistics and can be explained by Galactic foreground residuals, point-source residuals, or $1/f$ noise properties [Spergel *et al* (2006)]. Further tests on WMAP 3-year maps have found no significant deviation from Gaussianity.
From the WMAP 3-year sky maps, the constraint on f_{NL} is [Spergel *et al* (2006)]:

$$-54 < f_{NL} < 114$$

. Tests on other CMB experiments leads to similar results: Archeops [Curto *et al* (2006)], BOOMERanG [de Troia *et al* (2007)], MAXIMA [Cayón *et al* (2003)], VSA [Savage *et al* (2004), Rubiño-Martín *et al* (2006)].

13. Cosmological parameters estimation

Cosmological models, described by a given set of parameters, can predict the shape of the CMB angular power spectra. Thus, extracting cosmological information from CMB anisotropies means constraining the parameters of a model given the data. Maximum likelihood is often used as a method of parameter estimation to determine the best-fit model. Given a class of models and an observed data set, the probability distribution of the data (sometimes also multiplied by prior functions) is maximized as a function of the parameters. Then the goodness-of-fit must be constructed in order to decide if the best-fit model is indeed a good description of the data. If it is, one has to determine confidence intervals on the parameters estimation.
In principle, the likelihood function should be constructed using pixel map values. In most of standard inflationary scenarios, CMB fluctuations on the sky are Gaussian distributed, which implies that pixels are random variables following a multivariate normal distribution with a covariance matrix as a function of the model parameters and the noise. Since the parameters enter through the covariance matrix in a non-linear way, the likelihood function is not a linear function of the cosmological parameters. In practice, the complexity of this "full analysis" is increased by the size of the data set (million-pixel maps expected for Planck) and by the model calculations [Bond *et al* (1998), Bond *et al* (2000), Borrill (1999c), Kogut (1999)]. Thus, the angular power spectrum is preferred, as it reduces significantly the size of the data set without any loss of information, for the case of Gaussian fluctuations.
The exact meaning of the confidence intervals depends heavily on the method used:

- Marginalization: based on exact prediction of the Bayes theorem. For a given parameter, the probability is integrate over all the others

  $$\mathcal{P}(\theta_i) = \int d\theta_{n\neq i} \mathcal{L}(\theta_n)$$

  It answers to the question : "For a given value of θ, how good a fit can we get?"
- Minimization:

  $$\mathcal{P}(\theta_i) = max\left\{\mathcal{L}(\theta_n)\right\}_{n\neq i}$$

  It answers to the question : "Is there at least one good fit for this value of θ?"

Note that these two approaches are equivalent for a gaussian distribution of the parameters.
In both cases, finding the maximum of the likelihood surface in a multi-dimensional space is very computationally heavy to compute. Cosmological parameter estimators solve the problem by discretizing the space. For each set of parameters in a predetermined grid, they can store either all statistical information or only the likelihood value, $\mathcal{L}$, before marginalizing or minimizing. Recently, Markov Chains Monte Carlo (MCMC) likelihood analyses have become an alternative to these gridding

methods [Christensen & Meyer (2001), Lewis & Bridle (2002)]. This method is based on random draws of the distribution function that is supposed to be a "realistic" sample of the likelihood hypersurface. On this sample, one can derived the mean, variance and confidence levels. It allows a faster analysis: while the gridding methods scale exponentially with the number of parameters, the MCMC method scales linearly.

Historically, parameter estimation from CMB anisotropies started with a small number of free parameters (less than 5), all others assumed fixed to their nominal values. Now, the usual minimum set of parameter is made of 5: density of baryons (Ω_b), density of dark matter (Ω_{DM}), density of dark energy (Ω_Λ), amplitude of fluctuations (A) and the optical depth of rionization τ. To this minimal set can be added a lot of more specific parameters such as: the scalar index (n_s), the running index, dark energy equation of state (w) and its derivative, the neutrino masses, etc. In parallel, more and more observational data sets are included in the analysis coming from Supernovae Ia, Weak lensing, Baryon Acoustic Oscillations (BAO), Hubble constant measurement by HST, etc. The increase of complexity in the parameter estimation process has been allowed by the increase of computer speed as well as by the development of faster codes to compute the power spectra (CMBFAST [Seljak & Zaldarriaga (1996)]).

14. Current status of observations

Between the first COBE/DMR CMB anisotropy detection in 1992 and the recent WMAP detections, many sub-orbital experiments have measured the CMB anisotropies. In temperature, with WMAP [Hinshaw *et al* (2006)], BOOMERanG [Jones *et al* (2006)], Acbar, CBI and the VSA measurements, we have now a precise measurement of the angular power spectrum including the third acoustic peak. For polarization measurements, spectra are just now becoming available (from WMAP [Page *et al* (2006)], BOOMERanG [Piacentini *et al* (2006), Montroy *et al* (2006)]), DASI [Leitch *et al* (2005)], CBI [Readhead *et al* (2004)] and CAPMAP [Barkats *et al* (2005)]).

14.1. Angular power spectra

In 1992, the FIRAS instrument on the COBE satellite measured the CMB black body spectrum at $T = 2.735 \pm 0.06$ K [Mather *et al* (1990)] (updated in 2002 at $T = 2.725 \pm 0.001$ K [Fixsen & Mather (2002)]). With 7 degree angular resolution, DMR, its sister experiment on the satellite, constrained the low part ($\ell < 12$) of the temperature power spectra ([Gorski *et al* (1994)] and [Gorski *et al* (1996), Tegmark (1996a)]). Since then a number of experiments, both ground-based and balloon-borne, have helped refine our knowledge of the shape of the first acoustic peak.

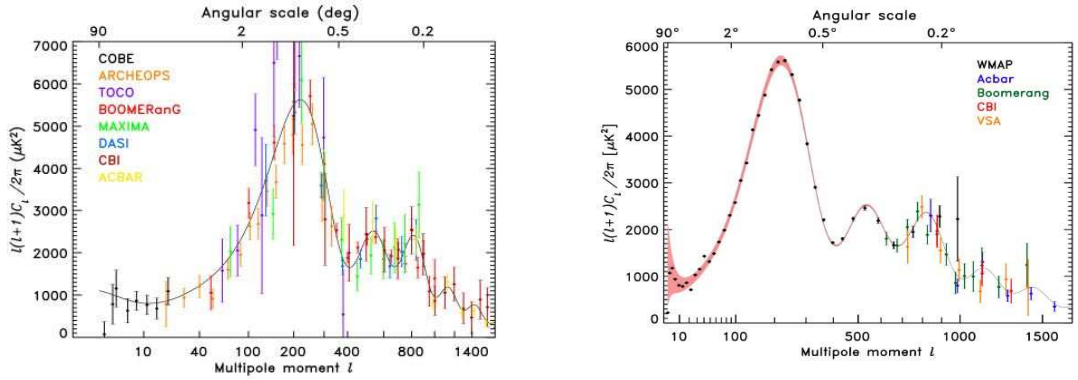

Figure 20. *Left:* CMB temperature angular power spectrum before WMAP in 2003 (COBE [Tegmark (1996a)], Archeops [Benoît *et al* (2003)], TOCO [Miller *et al* (2002)], BOOMERanG98 [Ruhl *et al* (2003)], Maxima01 [Lee *et al* (2001)], DASI [Halverson *et al* (2002)], CBI [Pearson *et al* (2003)] and ACBAR [Kuo *et al* (2004)]). (extracted from [Hinshaw *et al* (2003)]) *Right:* Results from the 3 years observation of WMAP [Hinshaw *et al* (2006)] together with last results from high resolution experiments: BOOMERanG [Jones *et al* (2006)], Acbar [Kuo *et al* (2004)], CBI [Readhead *et al* (2004)] and VSA [Dickinson *et al* (2004)]. (extracted from [Hinshaw *et al* (2006)])

Even before WMAP results were released, experiments when combined clearly showed the presence of the two acoustic peak (figure 20). But the error bars were still dominated by systematic effects, and calibration was very difficult to obtain from a data set where the instruments, the resolution and the frequency bands where so different. Some where dedicated to small angular scales using a high resolution on a small sky patches, such as DASI or CBI, whereas others, such as Archeops, covered large portions of the sky (30%).

Parameter	WMAP Only	WMAP +CBI+VSA	WMAP+ACBAR +BOOMERanG
$100\Omega_b h^2$	$2.233^{+0.072}_{-0.091}$	$2.212^{+0.066}_{-0.084}$	$2.231^{+0.070}_{-0.088}$
$\Omega_m h^2$	$0.1268^{+0.0072}_{-0.0095}$	$0.1233^{+0.0070}_{-0.0086}$	$0.1259^{+0.0077}_{-0.0095}$
h	$0.734^{+0.028}_{-0.038}$	$0.743^{+0.027}_{-0.037}$	$0.739^{+0.028}_{-0.038}$
A	$0.801^{+0.043}_{-0.054}$	$0.796^{+0.042}_{-0.052}$	$0.798^{+0.046}_{-0.054}$
τ	$0.088^{+0.028}_{-0.034}$	$0.088^{+0.027}_{-0.033}$	$0.088^{+0.030}_{-0.033}$
n_s	$0.951^{+0.015}_{-0.019}$	$0.947^{+0.014}_{-0.017}$	$0.951^{+0.015}_{-0.020}$
σ_8	$0.744^{+0.050}_{-0.060}$	$0.722^{+0.043}_{-0.053}$	$0.739^{+0.047}_{-0.059}$
Ω_m	$0.238^{+0.030}_{-0.041}$	$0.226^{+0.026}_{-0.036}$	$0.233^{+0.029}_{-0.041}$

Table 1. Cosmological parameters estimated using the 3-year WMAP data and some additional data from other CMB experiments (results extracted from [Spergel *et al* (2006)]).

In 2003, WMAP first year results [Bennett *et al* (2003a)], with improved sensitivity and sky coverage, gave error bars dominated by cosmic variance up to the second acoustic peak.
The first measurement of E-mode polarization was published by DASI in 2002 [Kovac *et al* (2002)], confirmed by the same team in 2004 [Leitch *et al* (2005)] as well as by CBI [Readhead *et al* (2004)] and CAPMAP [Barkats *et al* (2005)] (figure 21).

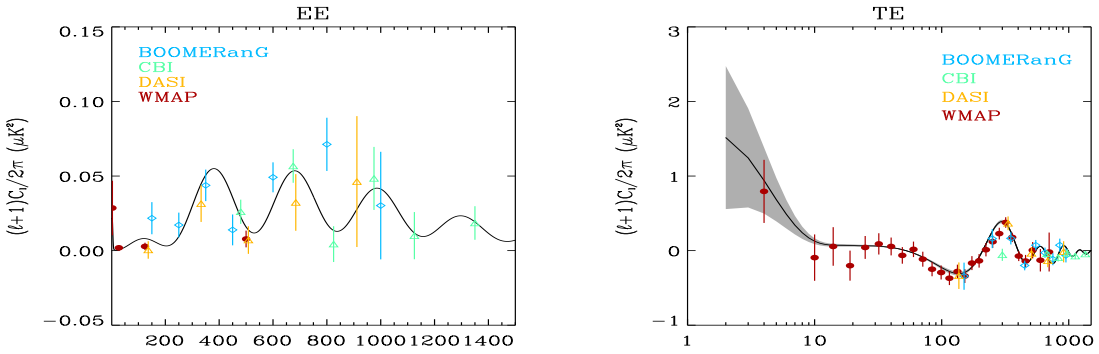

Figure 21. E-mode spectrum (*left*) and TE (*right*) measured by BOOMERanG [Montroy *et al* (2006), Piacentini *et al* (2006)], DASI [Leitch *et al* (2005)], CBI [Readhead *et al* (2004)] and WMAP [Page *et al* (2006), Hinshaw *et al* (2006)].

We have only two measurements for the cross-correlation TE spectrum (WMAP [Hinshaw *et al* (2006)] and BOOMERanG [Piacentini *et al* (2006)]). To this point, we only have upper limits for B-mode spectrum. This illustrates how complex CMB polarization detection is.

14.2. Cosmological parameters

The standard ΛCDM cosmological model agrees well with the most recent experimental results. Fewer than ten free parameters allow us to fit the bulk of high precision data. Under such conditions, CMB data put strong constraints on models with adiabatic perturbations with close to scale invariant initial conditions, with a nearly flat geometry and containing Dark Matter and Dark Energy. The CMB can provide constraints on a large set of parameters and, in conjunction with other astronomical measurements, it places significant limits on the geometry of the universe, the nature of dark energy, and even neutrino properties.
In [Spergel *et al* (2006)], the WMAP team fits a 6-parameter family of models (which fixes $\Omega_{tot} = 1$ and $r = 0$), together with weak priors (on h and $\Omega_b h^2$ for example). The estimated parameters are matter density ($\Omega_m h^2$), baryon density ($\Omega_b h^2$), Hubble Constant (H_0), amplitude of fluctuations (σ_8), optical depth (τ), and a slope for the scalar perturbation spectrum (n_s). The fit to the 3-year WMAP data combined with other CMB experiments yields the results in table 1.
Without spatial flatness, the CMB data alone provide only a very weak constraint for h. Inversely, including a prior on h from HST [Freedman *et al* (2001)] gives the best constraint on $\Omega_{tot} = 1.003^{+0.013}_{-0.017}$, although similar results come from using Supernova Legacy Survey data [Astier *et al* (2006)] or large-scale structure data.

The addition of other cosmological data-sets allows constraints to be placed on further parameters. Indeed, additional data are able to break degeneracies that exist using CMB data alone. For example, considering the dark energy equation of state w adds a degeneracy in the (w, h)-space for low values of both parameters. This can be broken using supernovae and large-scale structure data to yield $w = -1.06^{+0.13}_{-0.08}$.
In addition, CMB data can put limits on parameters relevant to particle physics models. In particular, the CMB allows us to derive strong constraints on the sum of neutrino masses from the neutrino density $\Omega_\nu h^2$, assuming the usual number density of fermions which decoupled when they were relativistic. CMB data alone place a limit on the neutrino mass of $m < 2.0$ eV (95% confidence) [Ichikawa *et al* (2005)]. Combining the CMB with other astrophysical observable (galaxy clustering, supernovae data, baryon acoustic oscillations, HST) reduce the upper bound by roughly one order of magnitude and gives the strongest constraint on the sum of neutrino masses [Fogli *et al* (2006), Kristiansen *et al* (2006), Seljak *et al* (2006)].

Acknowledgments

We acknowledge the use of the Legacy Archive for Microwave Background Data Analysis (LAMBDA). Support for LAMBDA is provided by the NASA Office of Space Science. We would like to thank Professor J. Silk.

Contents

[Acquaviva *et al* (2003)] Acquaviva V, Bartolo N, Matarrese S & Riotto A 2003 Nuclear Physics B **667** 119
[Alpher & Herman (1948)] Alpher R & Herman R 1948 Nature **162** 774
[Amblard & Hamilton (2004)] Amblard A & Hamilton J C 2004 A&A **417** 1189
[Ansari *et al* (2003)] Ansari R *et al* 2003 MNRAS **343** 552
[Armitage & Wandelt (2004)] Armitage C & Wandelt B D 2004 Phys. Rev. D **70** 123007
[Arnau & Saez (2000)] Arnau J V & Saez D 2000 New Astronomy **5** 121
[Ashdown *et al* (2006a)] Ashdown M A J *et al* 2006 *in preparation*
[Ashdown *et al* (2006b)] Ashdown M A J *et al* 2006 A&A *submitted*
[Astier *et al* (2006)] Astier P *et al* 2006 A&A **447** 31
[Aumont & Macías-Pérez (2007)] Aumont J & Macías-Pérez J F 2007 MNRAS **376** 739
[Baccigalupi *et al* (2004)] Baccigalupi C *et al* 2004 MNRAS **354** 55
[Barkats *et al* (2005)] Barkats D *et al* 2005 ApJ **619** L127
[Barnes (2003)] Barnes C *et al* 2003 ApJS **148** 51
[Bennett *et al* (2003a)] Bennett C L *et al* 2003 ApJS **148** 1
[Bennett *et al* (2003b)] Bennett C L *et al* 2003 ApJS **148** 97
[Benoît *et al* (2002)] Benoît A *et al* 2002 Astroparticle Physics **17** 101
[Benoît *et al* (2003)] Benoît A *et al* 2003 A&A **399** L19
[Benoît *et al* (2004)] Benoît A *et al* 2004 A&A **424** 571
[Bersanelli & Mandolesi (2000)] Bersanelli M & Mandolesi N 2000 Astroph. Lett. & Comm. **37** 171
[Bond *et al* (1998)] Bond J R, Jaffe A H and Knox L 1998 Phys. Rev. D **57** 2117
[Bond *et al* (2000)] Bond J R , Jaffe A H & Knox L 2000 ApJ **533** 19
[Borrill (1999a)] Borrill J 1999a Phys. Rev. D **59** 27302
[Borrill (1999b)] Borrill J 1999b *EC-TMR Conf. Proc. 476, 3K Cosmology* (eds. L. Maiani, F. Melchiorri and N. Vittorio, Woodbury AIP) p 277
[Borrill (1999c)] Borrill J 1999c *Proceedings of the 5th European SGI/Cray MPP Workshop* (*Preprint* astro-ph/9911389)
[Borrill (2007)] Borrill J D *et al* 2007 *in preparation*
[Bouchet *et al* (1999)] Bouchet F R *et al* 1999 MNRAS **302** 663
[Bouchet & Gispert (1999)] Bouchet F R & Gispert R 1999 New Astronomy **4** 443
[Boughn *et al* (1992)] Boughn S P, Cheng E S, Cottingham D A and Fixsen D J 1992 ApJ **391L** 49B
[Brown *et al* (2005)] Brown M L, Castro P G & Taylor A N 2005 MNRAS **360** 1262
[Burigana *et al* (1997)] Burigana C *et al* 1997 Int. Rep. TeSRE/CNR 198 (*Preprint* astro-ph/0307515)
[Burigana & Sáez (2003)] Burigana C & Sáez D 2003 A&A **409** 423
[Cayón *et al* (2003)] Cayón L, Argüeso F, Martínez-González E & Sanz J L 2003 MNRAS **344** 917
[Challinor & Chon (2005)] Challinor A D & Chon G 2005 MNRAS **360** 509
[Challinor *et al* (2002)] Challinor A D *et al* 2002 MNRAS **331** 994
[Chanin & Torre (1983)] Chanin G & Torren J P 1983 J. Opt. Soc. Am. A Opt. image sci. **1** 412
[Chon *et al* (2004)] Chon G *et al* 2004 MNRAS **350** 914
[Christensen & Meyer (2001)] Christensen N & Meyer R 2001 Phys. Rev. D **64** 22001
[Copi *et al* (2004)] Copi C J, Huterer D & Starkman G D 2004 Phys. Rev. D **70** 043515
[Crill (2001)] Crill B P 2001 *Ph. D. thesis* (Caltech)
[Crill *et al* (2003)] Crill B P *et al* 2003 ApJS **148** 527
[Cruz *et al* (2005)] Cruz M, Martínez-González E, Vielva P & Cayón L 2005 MNRAS **356** 29
[Curto *et al* (2006)] Curto A, Aumont J, Macias-Perez J F, Martinez-Gonzalez E, Barreiro R B, Santos D & Desert F X 2006 ArXiv Astrophysics e-prints (*Preprint* astro-ph/0612148)
[de Gasperis *et al* (2005)] de Gasperis *et al* 2005 A&A **436** 1159
[Delabrouille *et al* (1998)] Delabrouille J 1998 A&AS **127** 555
[Delabrouille *et al* (2003)] Delabrouille J , Cardoso J -F and Patanchon G 2003 MNRAS **346** 1089
[de Troia *et al* (2007)] de Troia G *et al* 2007 New Astronomy Review **51** 250
[de Zotti *et al* (1999)] de Zotti G *et al* 1999 AIP Conf. Proc. **476** 204
[Dicke *et al* (1946)] Dicke R H 1946 Rev. Sci. Instrum. **17** 268
[Dicke *et al* (1965)] Dicke R H, Peebles P J E, Roll P G & Wilkinson D T 1965 ApJ **142** 414
[Dickinson *et al* (2004)] Dickinson C *et al* 2004 MNRAS **353** 732
[Doré *et al* (2001)] Dor O *et al* 2001 A&A **374** 358
[Efstathiou (2004)] Efstathiou G 2004 MNRAS **349** 603
[Efstathiou (2006)] Efstathiou G 2006 MNRAS **370** 343
[Eriksen *et al* (2004a)] Eriksen H K *et al* 2004 ApJ **612** 633
[Eriksen *et al* (2004b)] Eriksen H K *et al* 2004 ApJS155 227
[Eriksen *et al* (2004c)] Eriksen H K, Hansen F K, Banday A J, Górski K M & Lilje P B 2004 ApJ **605** 14
[Ferreira & Jaffe (2000)] Ferreira P G & Jaffe A H 2000 MNRAS **312** 89
[Finkbeiner *et al* (1999)] Finkbeiner D P *et al* 1999 ApJ **524** 867
[Fixsen & Mather (2002)] Fixsen D J & Mather J C 2002 ApJ **581** 817
[Fogli *et al* (2006)] Fogli G L *et al* 2007 Phys. Rev. D **75** 053001
[Fosalba *et al* (2002)] Fosalba P *et al* 2002 Phys. Rev. D **65** 063003
[Freedman *et al* (2001)] Freedman W L *et al* 2001 ApJ **553** 47
[Ganga *et al* (1993)] Ganga K, Cheng E, Meyer S and Page L 1993 ApJ **410L** 57
[Giardino *et al* (2002)] Giardino G *et al* 2002 A&A **387** 82
[Golub & van Loan (1996)] Golub G H & van Loan C F 1996 *Matrix Computations* 3rd edition (John Hopkins University Press)
[Gorski *et al* (1994)] Górski K M *et al* 1994 ApJ **430** L89
[Gorski *et al* (1996)] Górski K M *et al* 1996 ApJ **464** L11
[Gorski *et al* (2005)] Górski K M *et al* 2005 ApJ **622** 759
[Gunn & Peterson (1965)] Gunn J E & Peterson B A 1965 ApJ **142** 1633
[Halverson *et al* (2002)] Halverson N W *et al* 2002 ApJ **568** 38
[Hansen & Górski (2003)] Hansen F and Górski K M 2003 MNRAS **343** 559
[Hansen *et al* (2004)] Hansen F K, Cabella P, Marinucci D & Vittorio N 2004 ApJ **607** L67

[Harrison (2004)] Harrison D L, van Leewen F & Rowan-Robison M 2004 MNRAS **348** 1241
[Hinderks (2005)] Hinderks J 2005 *Ph.D. Thesis* (Stanford University)
[Hinshaw *et al* (2003)] Hinshaw G *et al* 2003 ApJS **148** 135
[Hinshaw *et al* (2006)] Hinshaw G *et al* 2006 submitted to ApJ
[Hivon *et al* (2002)] Hivon E *et al* 2002 ApJ **567** 2
[Hobson & Lasenby (1998)] Hobson M P & Lasenby A N 1998 MNRAS **298** 905
[Hobson & Mageuijo (1996)] Hobson M P & Mageuijo J 1996 MNRAS **283** 1133
[Hubble (1929)] Hubble E 1929 Proc. Natl. Acad. Sci. **15** 168
[Hu *et al* (1995a)] Hu W, Scott D, Sugiyama N and White M 1995 Phys. Rev. D **52** 5498
[Hu *et al* (1997)] Hu W, Spergel D N and White M 1997 Phys. Rev. D **55** 3288
[Ichikawa *et al* (2005)] Ichikawa K, Fukugita M & Kawasaki M 2005 Phys. Rev. D **71** 043001
[Janssen *et al* (1996)] Janssen M A *et al* 1996 ArXiv Astrophysics e-prints (*Preprint* astro-ph/9602009)
[Jarosik *et al* (2003)] Jarosik N *et al* 2003 ApJS **145** 413
[Jarosik *et al* (2006)] Jarosik N *et al* 2006 ApJ *submitted*
[Jewell *et al* (2004)] Jewell J, Levin S & Anderson C H 2004 ApJ **609** 1
[Jones *et al* (2003)] Jones W C *et al* 2003 Proc. SPIE **4855** 227
[Jones *et al* (2006)] Jones W C *et al* 2006 ApJ **647** 823J
[Kalman (1960)] Kalman R E 1960 Journal of Basic Engineering **82D** 35
[Keihanen *et al* (2004)] Keihänen E *et al* 2004 A&A **428** 287
[Keihanen *et al* (2005)] Keihänen E *et al* 2005 MNRAS **360** 390
[Keihanen *et al* (2007)] Keihänen E *et al* 2007 *in preparation*
[Knox (1995)] Knox L 1995 Phys. Rev. D **52** 4307
[Kogut (1999)] Kogut A 1999 ApJ **520** L83
[Kogut *et al* (2003)] Kogut A *et al* 2003 ApJS **148** 161
[Kovac *et al* (2002)] Kovac J *et al* 2002 Nature **420** 772
[Kristiansen *et al* (2006)] Kristiansen J R *et al* 2006 ArXiv Astrophysics e-prints (*Preprint* astro-ph/0611761)
[Kuo *et al* (2004)] Kuo C L *et al* 2004 ApJ **600** 32
[Landriau & Shellard (2003)] Landriau M & Shellard E P S 2003 PRD **67** 103512
[Lee *et al* (2001)] Lee A T *et al* 2001 ApJ **561** L1
[Leitch *et al* (2005)] Leitch E *et al* 2005 ApJ **624** 10L
[Lewis & Bridle (2002)] Lewis A & Bridle S 2002 Phys. Rev. D **66** 103511
[Liddle & Lyth (2000)] Liddle A R and Lyth D H 2000 *Cosmological Inflation and Large-Scale Structure* (Cambridge University Press, Cambridge)
[Linde *et al* (1999)] Linde A, Sasaki M, Tanaka T 1999 Phys. Rev. D **59** 123522
[Lineweaver (1997)] Lineweaver C H 1997 Astronomical Society of the Pacific Conference Series **126** 185
[Macías-Pérez & Bourrachot (2006)] Macías-Pérez J F *et al* 2006 A&A **459** 987
[Macías-Pérez *et al* (2007)] Macías-Pérez J F *et al* 2007 A&A **467** 1313
[Maino *et al* (1999)] Maino D *et al* 1999 A&AS **140** 383
[Maino *et al* (2002a)] Maino D, Burigana C, Gorski K M, Mandolesi N and Bersanelli M 2002 A&A **387** 356
[Maino *et al* (2002b)] Maino D *et al* 2002 MNRAS **334** 53
[Maldacena (2003)] Maldacena J 2003 JHEP **0305** 013
[Martin & Partridge (1988)] Martin H M & Partridge R B 1988 ApJ **324** 794
[Masi *et al* (2006)] Masi S *et al* 2006 A&A **458** 687
[Mather *et al* (1984)] Mather J C 1984 Appl. Opt. **23** 584
[Mather *et al* (1990)] Mather J C *et al* 1990 ApJ **354** L37
[Miller *et al* (2002)] Miller A D *et al* 2002 ApJS **140** 115
[Montroy *et al* (2006)] Montroy T E *et al* 2006 ApJ **647** 813M
[Muciaccia *et al* (1997)] Muciaccia P F, Natoli P and Vittorio N *et al* 1997 ApJ **488** L63
[Natoli *et al* (2001)] Natoli P *et al* 2001 A&A **372** 346
[Natoli *et al* (2002)] Natoli P *et al* 2002 A&A **383** 1100
[O'Dwyer *et al* (2004)] O'Dwyer I J *et al* 2004 ApJ **617** L99
[Page *et al* (2003)] Page L *et al* 2003 ApJS **148** 39
[Page *et al* (2006)] Page L *et al* 2006 ApJ submitted
[Park *et al* (2003)] Park C G, Ng K W, Park C, Liu G C & Umetsu K 2003 ApJ **589** 67
[Park (2004)] Park C 2004 MNRAS **349** 313
[Pearson *et al* (2003)] Pearson T J *et al* 2003 ApJ **591** 556
[Peebles (1973)] Peebles P J E 1973 ApJ **185** 431
[Peebles & Hauser (1974)] Peebles P J E and Hauser M G 1974 ApJS **28** 19
[Penzias & Wilson (1965)] Penzias A A and Wilson R W ApJ **142** 419
[Perdereau *et al* (2007)] Perdereau O *et al* 2007 in preparation
[Piacentini *et al* (2006)] Piacentini F *et al* 2006 ApJ **647** 833P
[Ponthieu *et al* (2005)] Ponthieu N, Macias-Perez J-F, Tristram M *et al* 2005 A&A **444** 327
[Poutanen *et al* (2006)] Poutanen T *et al* A&A **449** 1311
[Rabii *et al* (2006)] Rabii B *et al* 2006 Rev. Sci. Instrum. **77** 071101
[Rajguru *et al* (2005)] Rajguru N *et al* 2005 MNRAS **363** 1125
[Readhead *et al* (2004)] Readhead A *et al* 2004 Science **306** 836
[Rees & Sciama (1968)] Rees M J & Sciama D W 1968 Nature **511** 611
[Rubiño-Martín *et al* (2006)] Rubiño-Martín J A, Aliaga A M, Barreiro R B *et al* 2006 MNRAS **369** 909
[Ruhl *et al* (2003)] Ruhl J E *et al* 2003 ApJ **599** 786
[Sachs & Wolfe (1967)] Sachs R K & Wolfe A M 1967 ApJ **147** 73
[Savage *et al* (2004)] Savage R *et al* 2004 MNRAS **349** 973
[Schlegel *et al* (1998)] Schlegel D, Finkbeiner D and Davis M 1998 ApJ **500** 525
[Scott *et al* (1994)] Scott P F *et al* 1994 ApJ **421** L5
[Seljak (1996)] Seljak U 1996 ApJ **436** 509
[Seljak & Zaldarriaga (1996)] Seljak U & Zaldarriaga M 1996 ApJ **469** 437

[Seljak & Zaldarriaga (2000)] Seljak U & Zaldarriaga M 2000 ApJ **538** 57
[Seljak *et al* (2006)] Seljak U, Slosar A and McDonald P 2006 Journal of Cosmology and Astro-Particle Physics **10** 14
[Smoot (1990)] Smoot G *et al* 1990 ApJ **360** 685
[Souradeep & Ratra (2001)] Souradeep T & Ratra B 2001 ApJ **560** 28
[Spergel *et al* (2006)] Spergel D N *et al* 2006 ApJ *submitted*
[Stompor *et al* (2002)] Stompor R *et al* 2002 Phys. Rev. D**65** 022003
[Subrahmanyan *et al* (1993)] Subrahmanyan R *et al* 1993 MNRAS **263** 416
[Szapudi *et al* (2001)] Szapudi I *et al* 2001 ApJ **548** L115
[Tanner (1996)] Tanner M A 1996 *Tools for statistical inference* (3rd e. Springer-Verlag, New York)
[Tegmark (1996a)] Tegmark M 1996 ApJ **464** L35
[Tegmark (1996b)] Tegmark M 1996 MNRAS **280** 299
[Tegmark (1997)] Tegmark M 1997 Phys. Rev. D **55** 5895
[Tegmark & de Oliveira-Costa (2001)] Tegmark M and de Oliveira-Costa A 2001 Phys. Rev. D **64** 63001
[Tegmark *et al* (2003)] Tegmark M, de Oliveira-Costa A, & Hamilton A J 2003 Phys. Rev. D **68** 123523
[Tompson *et al* (1986)] Tompson A R, Moran J M and Swenson G W 1986 *Interferometry and Sunthesis in Radio Astronomy* (New York: Wiley)
[Tristram *et al* (2004)] Tristram M, Hamilton J-Ch, Macías-Peréz J F and Renault C 2004 Phys. Rev. D **69** 123008
[Tristram *et al* (2005a)] Tristram M *et al* 2005 MNRAS **358** 833
[Tristram *et al* (2005b)] Tristram M *et al* 2005 A&A **436** 785
[van Leeuwen *et al* (2002)] van Leeuwen F *et al* 2002 MNRAS **331** 975
[Vielva *et al* (2004)] Vielva P, Martínez-González E, Barreiro R B, Sanz J L & Cayón L 2004 ApJ**609** 22
[Wandelt *et al* (2001)] Wandelt B D, Hivon E and Gorski K M 2001 Phys. Rev. D **64** 083003
[Wandelt *et al* (2004)] Wandelt B D, Larson D L & Lakshminarayanan A 2004 Phys. Rev. D **70** 083511
[Wandelt & Hansen (2003)] Wandelt B D & Hansen F K 2003 Phys. Rev. D **67** 023001
[Wands *et al* (2002)] Wands D, Bartolo N, Matarrese S & Riotto A 2002 PRD **66** 043520
[Watson *et al* (2005)] Watson R A *et al* 2005 ApJ **624** L89
[White (1999)] White M *et al* 1999 ApJ **514** 12
[Wright (1996)] Wright E L 1996 ArXiv Astrophysics e-prints (*Preprint* astro-ph/9612006)
[Wu *et al* (2001)] Wu J H P *et al* 2001 ApJS **132** 1
[Yvon & Mayet (2005)] Yvon D & Mayet F 2005 A&A **436** 729
[Zaldarriaga (2002)] Zaldarriaga M 2002 *Pasadena 2002, Measuring and modeling the universe* (Cambridge University Press) p 309-329 (*Preprint* astro-ph/0305272)
[Zel'dovich & Sunyaev (1969)] Zel'dovich Y B and Sunyaev R A 1969 Ap&SS **4** 301